

NUREG/CR-6317
UILU-ENG-95-2001

Numerical Investigation of 3-D Constraint Effects on Brittle Fracture in SE(B) and C(T) Specimens

RECEIVED
AUG 20 1996

OSTI

Prepared by
Markku Nevalainen, TRCF (VTT)
R. H. Dodds, Jr., UI

Technical Research Centre of Finland (VTT)

University of Illinois

Naval Surface Warfare Center

Prepared for
U.S. Nuclear Regulatory Commission

DISTRIBUTION OF THIS DOCUMENT IS UNLIMITED

RB

MASTER

AVAILABILITY NOTICE

Availability of Reference Materials Cited in NRC Publications

Most documents cited in NRC publications will be available from one of the following sources:

1. The NRC Public Document Room, 2120 L Street, NW., Lower Level, Washington, DC 20555-0001
2. The Superintendent of Documents, U.S. Government Printing Office, P. O. Box 37082, Washington, DC 20402-9328
3. The National Technical Information Service, Springfield, VA 22161-0002

Although the listing that follows represents the majority of documents cited in NRC publications, it is not intended to be exhaustive.

Referenced documents available for inspection and copying for a fee from the NRC Public Document Room include NRC correspondence and internal NRC memoranda; NRC bulletins, circulars, information notices, inspection and investigation notices; licensee event reports; vendor reports and correspondence; Commission papers; and applicant and licensee documents and correspondence.

The following documents in the NUREG series are available for purchase from the Government Printing Office: formal NRC staff and contractor reports, NRC-sponsored conference proceedings, international agreement reports, grantee reports, and NRC booklets and brochures. Also available are regulatory guides, NRC regulations in the *Code of Federal Regulations*, and *Nuclear Regulatory Commission Issuances*.

Documents available from the National Technical Information Service include NUREG-series reports and technical reports prepared by other Federal agencies and reports prepared by the Atomic Energy Commission, forerunner agency to the Nuclear Regulatory Commission.

Documents available from public and special technical libraries include all open literature items, such as books, journal articles, and transactions. *Federal Register* notices, Federal and State legislation, and congressional reports can usually be obtained from these libraries.

Documents such as theses, dissertations, foreign reports and translations, and non-NRC conference proceedings are available for purchase from the organization sponsoring the publication cited.

Single copies of NRC draft reports are available free, to the extent of supply, upon written request to the Office of Administration, Distribution and Mail Services Section, U.S. Nuclear Regulatory Commission, Washington, DC 20555-0001.

Copies of industry codes and standards used in a substantive manner in the NRC regulatory process are maintained at the NRC Library, Two White Flint North, 11545 Rockville Pike, Rockville, MD 20852-2738, for use by the public. Codes and standards are usually copyrighted and may be purchased from the originating organization or, if they are American National Standards, from the American National Standards Institute, 1430 Broadway, New York, NY 10018-3308.

DISCLAIMER NOTICE

This report was prepared as an account of work sponsored by an agency of the United States Government. Neither the United States Government nor any agency thereof, nor any of their employees, makes any warranty, expressed or implied, or assumes any legal liability or responsibility for any third party's use, or the results of such use, of any information, apparatus, product, or process disclosed in this report, or represents that its use by such third party would not infringe privately owned rights.

Numerical Investigation of 3-D Constraint Effects on Brittle Fracture in SE(B) and C(T) Specimens

Manuscript Completed: February 1995
Date Published: July 1996

Prepared by
Markku Nevalainen, TRCF (VTT), R. H. Dodds, Jr., UI

Technical Research Centre of Finland (VTT)

Department of Civil Engineering
University of Illinois at Urbana Champaign
Urbana, IL 61801

Under contract to:
Naval Surface Warfare Center
3-A Leggett Circle
Annapolis, MD 21402-5067

S. N. Malik, NRC Project Manager

Prepared for
Division of Engineering Technology
Office of Nuclear Regulatory Research
U.S. Nuclear Regulatory Commission
Washington, DC 20555-0001
NRC Job Code J6036

DISCLAIMER

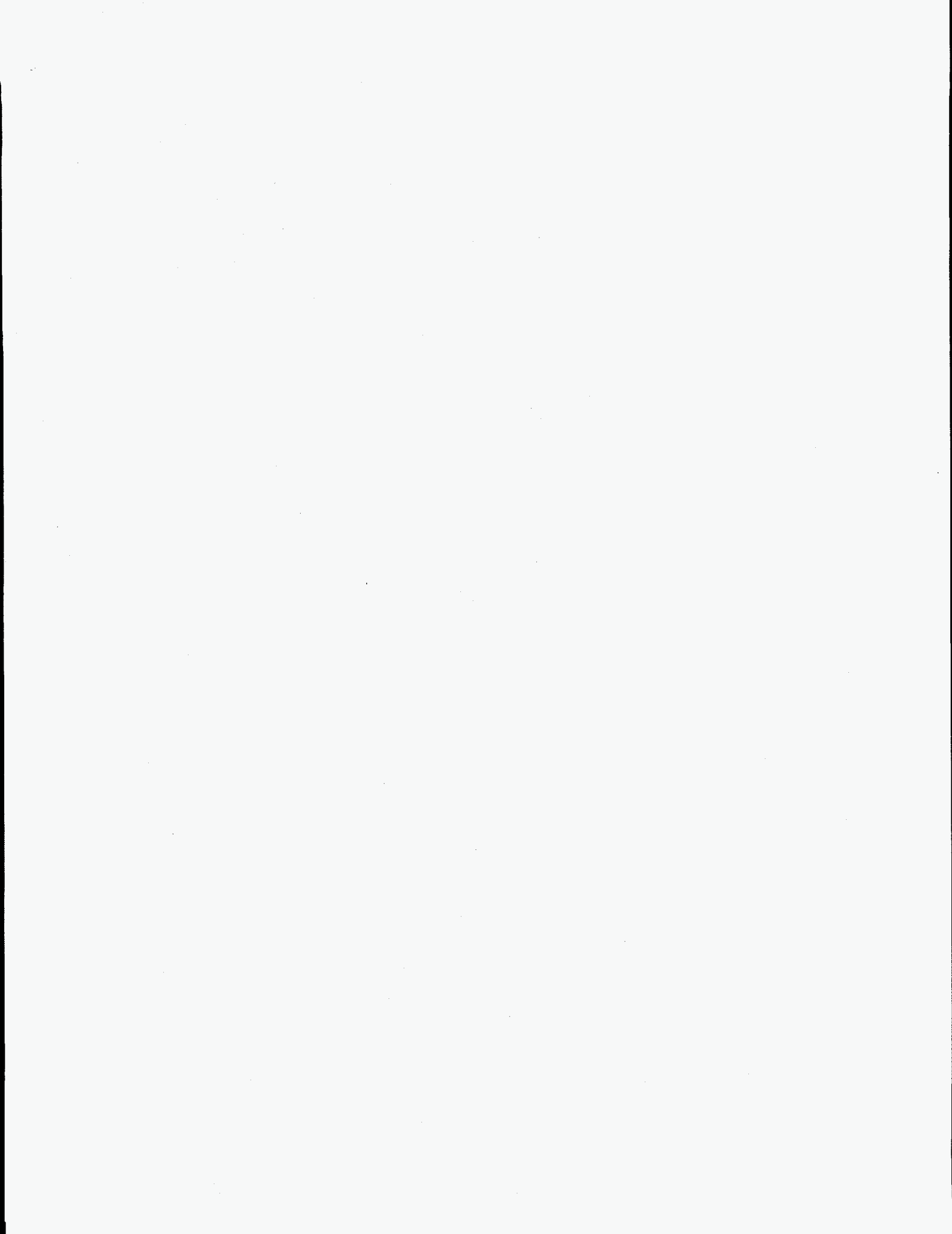
Portions of this document may be illegible in electronic image products. Images are produced from the best available original document.

DISCLAIMER

This report was prepared as an account of work sponsored by an agency of the United States Government. Neither the United States Government nor any agency thereof, nor any of their employees, makes any warranty, express or implied, or assumes any legal liability or responsibility for the accuracy, completeness, or usefulness of any information, apparatus, product, or process disclosed, or represents that its use would not infringe privately owned rights. Reference herein to any specific commercial product, process, or service by trade name, trademark, manufacturer, or otherwise does not necessarily constitute or imply its endorsement, recommendation, or favoring by the United States Government or any agency thereof. The views and opinions of authors expressed herein do not necessarily state or reflect those of the United States Government or any agency thereof.

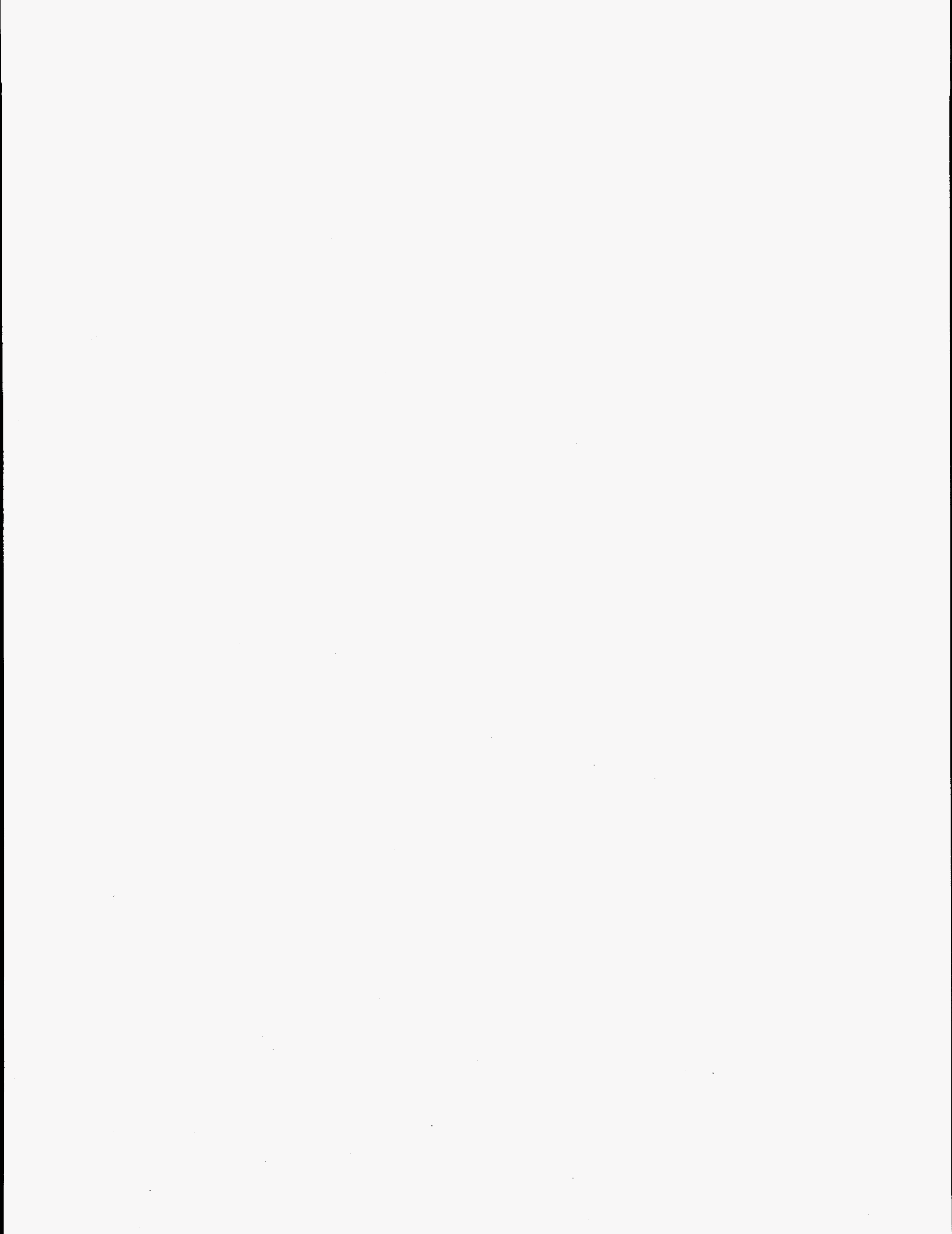
ABSTRACT

This investigation employs 3-D nonlinear finite element analyses to conduct an extensive parametric evaluation of crack front stress triaxiality for deep notch SE(B) and C(T) specimens and shallow notch SE(B) specimens, with and without side grooves. Crack front conditions are characterized in terms of J - Q trajectories and the constraint scaling model for cleavage fracture toughness proposed previously by Dodds and Anderson. The 3-D computational results imply that a significantly less strict size/deformation limit, relative to the limits indicated by previous plane-strain computations, is needed to maintain small-scale yielding conditions at fracture by a stress-controlled, cleavage mechanism in deep notch SE(B) and C(T) specimens. Additional new results made available from the 3-D analyses also include revised η -plastic factors for use in experimental studies to convert measured work quantities to thickness average and maximum (local) J -values over the crack front.



Contents

Section No.	Page
Abstract	iii
List of Figures	v
List of Tables	vii
Acknowledgements	viii
List of Prior Reports	ix
1. Introduction	1
2. Descriptions of Constraint and Statistical Effects	2
2.1 <i>J-Q</i> Theory	4
2.2 Toughness Scaling Model for Cleavage	5
2.3 Extensions for 3-D Configurations Including Statistical Effects	6
3. Computational Procedures	8
3.1 3-D Finite Element Models	8
3.2 Constitutive Model	8
3.3 Solution Procedures	9
3.4 SSY Boundary Layer Models	10
4. Results and Discussion	10
4.1 Global Response: <i>J</i> and CTOD Distributions Over the Crack Front	10
4.2 Crack Stress Triaxiality: <i>J-Q</i> Trajectories	12
4.3 Crack Stress Triaxiality: Toughness Scaling Model	13
4.4 Effective Thicknesses	15
5. Summary and Conclusions	16
6. References	16



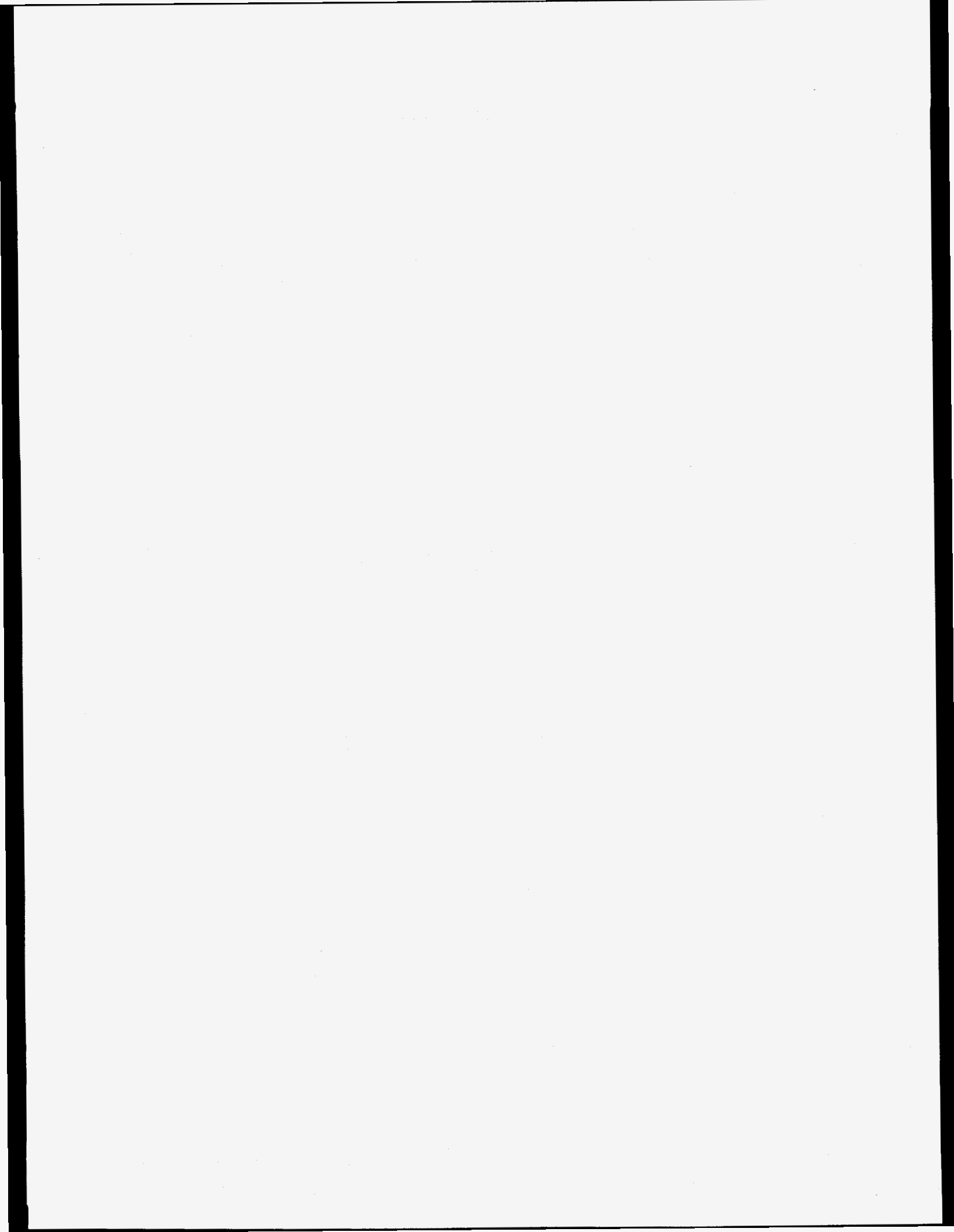
LIST OF FIGURES

Figure No.	Page
1	Typical finite element models for investigation of constraint effects in: (a) SE(B) specimens and (b) C(T) specimens. 25
2	Opening mode stresses on crack plane and principal stress contour areas for SSY ($T=0$, plane-strain). 26
3	a) Normalized load-displacement responses for deep notch SE(B) specimens. (b) Normalized plastic work on remaining ligament used to compute plastic "eta" factors for J estimation. $E/\sigma_0=500$, $n=10$ all analyses. 27
4	Distributions of J over crack front for shallow notch SE(B), $a/W=0.1$. (a) $W/B=2$, $n=5$; (b) $W/B=2$, $n=10$; (c) $W/B=1$, $n=5$; (d) $W/B=1$, $n=10$. $E/\sigma_0=500$, $\nu=0.3$ all analyses.. . . . 28
5	Distributions of J over crack front for C(T) specimens, $a/W=0.6$, $W/B=2$, $n=10$; (a) plane-sided specimen, (b) specimen with 20% side grooves. $E/\sigma_0=500$, $\nu=0.3$ all analyses.. . . . 29
6	Distributions of CTOD over crack front for plane-sided SE(B) specimens, $W/B=1$, $n=10$. (a) $a/W=0.5$, (b) $a/W=0.1$. $E/\sigma_0=500$, $\nu=0.3$ all analyses. 30
7	Constraint in terms of Q triaxiality parameter for plane-sided, deep and shallow notch SE(B) specimens having $W/B=1$, $n=10$. (a) and (b) show variations across crack front for Q defined at $r/(J/\sigma_0)=2$. (c) and (d) show typical dependence of Q on distance ahead of crack tip. $E/\sigma_0=500$, $\nu=0.3$ in all analyses. 31
8	J - Q trajectories for SE(B) specimens showing effects of a/W ratio, B/W ratio, side-grooves and strain hardening. Q defined at $r/(J/\sigma_0)=2$ and $E/\sigma_0=500$, $\nu=0.3$ in all analyses. 32
9	J - Q trajectories for C(T) specimens showing effects of B/W ratio, side-grooves and strain hardening. Q defined at $r/(J/\sigma_0)=2$ and $E/\sigma_0=500$, $\nu=0.3$ in all analyses.. . . . 33
10	Constraint in terms of the toughness scaling model for plane-sided, deep and shallow notch SE(B) specimens having $W/B=1$, $n=10$. (a) and (b) show variations across crack front. (c) and (d) show corresponding dependence of toughness scaling ratio on specified principal stress value. $E/\sigma_0=500$, $\nu=0.3$ in all analyses. 34
11	Constraint in terms of the toughness scaling model for plane-sided, deep and shallow notch SE(B) specimens having $W/B=2$, $n=10$. (a) and (b) show variations across crack front. (c) and (d) show corresponding dependence of toughness scaling ratio on specified principal stress value. $E/\sigma_0=500$, $\nu=0.3$ in all analyses. 35

12	Constraint in terms of the toughness scaling model for plane-sided, deep and shallow notch SE(B) specimens having $W/B = 1, n = 5$. (a) and (b) show variations across crack front. (c) and (d) show corresponding dependence of toughness scaling ratio on specified principal stress value. $E/\sigma_0 = 500, \nu = 0.3$ in all analyses.	36
13	Constraint in terms of the toughness scaling model for plane-sided, deep and shallow notch SE(B) specimens having $W/B = 2, n = 5$. (a) and (b) show variations across crack front. (c) and (d) show corresponding dependence of toughness scaling ratio on specified principal stress value. $E/\sigma_0 = 500, \nu = 0.3$ in all analyses.	37
14	Constraint in terms of the toughness scaling model for plane-sided C(T) specimens having $W/B = 2, a/W = 0.6$. (a) and (b) show variations across crack front. (c) and (d) show corresponding dependence of toughness scaling ratio on specified principal stress value. $E/\sigma_0 = 500, \nu = 0.3$ in all analyses.	38
15	Constraint in terms of the toughness scaling model for 20% side-grooved C(T) specimens having $W/B = 2, a/W = 0.6$. (a) shows variations across crack front. (b) shows corresponding dependence of toughness scaling ratio on specified principal stress value. $E/\sigma_0 = 500, \nu = 0.3$ in all analyses. ...	39
16	Areas within a principal stress contour across the crack front (a), (b) for plane-sided SE(B) specimens with $n = 10$. Effective thicknesses for deep and shallow notch configurations over a range of thicknesses and principal stress ratios (c), (d). $E/\sigma_0 = 500, \nu = 0.3$ in all analyses.	40
17	Effective thicknesses for deep notch C(T) and SE(B) specimens showing the effects of 20% side-grooves. $E/\sigma_0 = 500, \nu = 0.3, n = 10$ all analyses.	41
18	Comparison of effective and actual thicknesses for plane-sided SE(B) and C(T) specimens. $E/\sigma_0 = 500, \nu = 0.3$	42

LIST OF TABLES

Table No.		Page
1	Plastic η factors for SE(B) and C(T) specimens.	21
2	m -values for CTOD- J relationship: $J_{local} = m\sigma_{flow}\delta_{local}$	22
3	M factors for size/deformation limit in $b \geq MJ_{avg}/\sigma_0$	23
4	B_{eff} ratios at saturation and deformation levels.	24



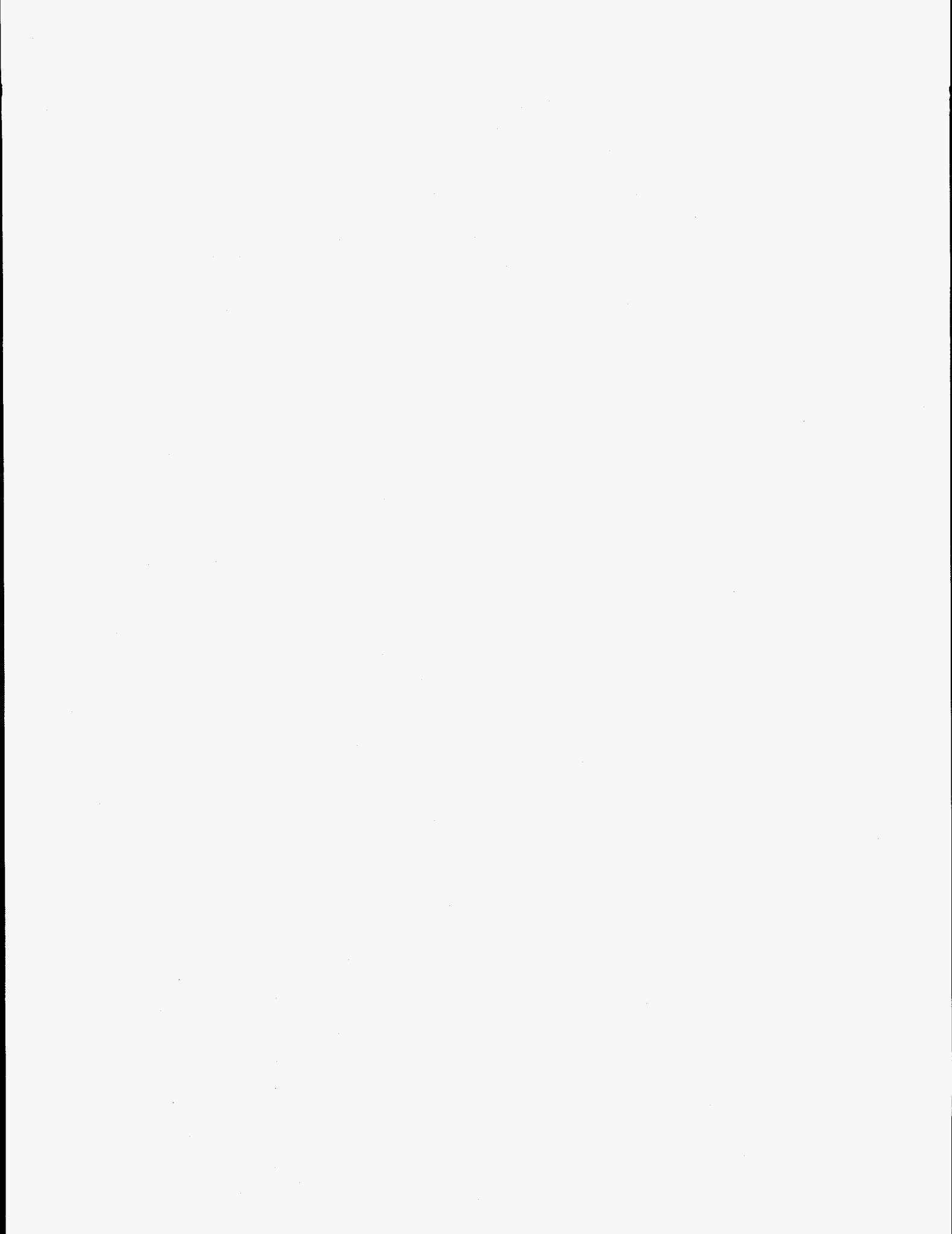
ACKNOWLEDGMENTS

This investigation was supported by grants principally from the U.S. Nuclear Regulatory Commission and the Naval Surface Warfare Center—Annapolis Detachment (Code 614).

The first author (MN) received partial support from the Technical Research Centre of Finland, the Finnish Academy and Foundations of Imatran Voima, W. Ahlstrom and Ella och Georg Ehrnrooth.

The authors acknowledge the many useful discussions and contributions of their colleagues Drs. Claudio Ruggieri (UIUC), Kim Wallin (VTT Finland) and Rick Link (NSWC).

Supercomputer access provided by the National Aerodynamic Simulator facility at NASA-Ames is gratefully acknowledged.



PRIOR REPORTS

Prior reports in this series are listed below:

1. J.A. Joyce, "Application of the Key Curve Method to Determining J - R Curves for A533B Steel," NUREG/CR-1290, U.S. Nuclear Regulatory Commission, Washington, DC (January 1980).
2. J.P. Gudas, M.G. Vassilaros, J.A. Joyce, D.A. Davis, and D.R. Anderson, "Summary of Recent Investigations of Compact Specimen Geometry Effects on the J_I - R Curve of High Strength Steels," NUREG/CR-1813, U.S. Nuclear Regulatory Commission, Washington, DC (November 1980).
3. J.A. Joyce, "Static and Dynamic J - R Curve Testing of A533B Steel Using the Key Curve Analysis Technique," NUREG/CR-2274, U.S. Nuclear Regulatory Commission, Washington, DC (July 1981).
4. J.A. Joyce, "Instability Testing of Compact and Pipe Specimens Utilizing a Test System Made Compliant by Computer Control," NUREG/CR-2257, U.S. Nuclear Regulatory Commission, Washington, DC (March 1982).
5. M.G. Vassilaros, J.P. Gudas, and J.A. Joyce, "Experimental Investigation of Tearing Instability Phenomena for Structural Materials," NUREG/CR-2570, Rev. 1, U.S. Nuclear Regulatory Commission, Washington, DC (August 1982).
6. Davis, D.A., Vassilaros, M.G., and Gudas, J.P., "Specimen Geometry and Extended Crack Growth Effects on J_I - R Curve Characteristics for HY-130 and ASTM A533B Steels," USNRC Report NUREG/CR-3089, U.S. Nuclear Regulatory Commission, Washington, DC (November 1982).
7. Vassilaros, M.G. et al., " J -Integral Tearing Instability for 8-Inch Diameter ASTM A106 Steel Pipe." USNRC Report NUREG/CR-3740, U.S. Nuclear Regulatory Commission, Washington, DC (March 1984).
8. J.A. Joyce, "Development and Verification of Conditions for Ductile Tearing Instability and Arrest," NUREG/CR-4528, U.S. Nuclear Regulatory Commission, Washington, DC (February 1986).
9. Hays, R.A., Vassilaros, M.G., and Gudas, J.P., "Fracture Analysis of Welded Type 304 Stainless Steel Pipe," USNRC Report NUREG/CR-4538 Vol. 1, U.S. Nuclear Regulatory Commission, Washington, DC (February 1986).
10. Link, R.E., and Hays, R.A., "Investigation of Tearing Instability Phenomena in ASTM A106 Steel," USNRC Report NUREG/CR-4539, U.S. Nuclear Regulatory Commission, Washington, DC (February 1986).
11. Hackett, E.M., Kirk, M.T., and Hays, R.A., "An Evaluation of J - R Curve Testing of Nuclear Piping Materials Using the Direct Current Potential Drop Technique," USNRC Report NUREG/CR-4540, U.S. Nuclear Regulatory Commission, Washington, DC (June 1986).
12. J.A. Joyce and E.M. Hackett, "Application of the Key Curve and Multispecimen Techniques to Dynamic J - R Curve Testing of Alloy Steel," NUREG/CR-4579, U.S. Nuclear Regulatory Commission, Washington, DC (April 1986).
13. J.A. Joyce and C.S. Schneider, "Application of Alternating Current Potential Difference to Crack Length Measurement During Rapid Loading," NUREG/CR-4699, U.S. Nuclear Regulatory Commission, Washington, DC (August 1986).
14. J.A. Joyce and E.M. Hackett, "Development of an Analytic Key Curve Approach to Drop Tower J - R Curve Measurement," NUREG/CR-4782, U.S. Nuclear Regulatory Commission, Washington, DC (December 1986).

15. J.A. Joyce and E.M. Hackett, "*Transition Range Drop Tower J-R Curve Testing of A106 Steel*," NUREG/CR-4818, U.S. Nuclear Regulatory Commission, Washington, DC (February 1987).
16. J.A. Joyce "*Ductile to Brittle Toughness Transition Characterization of A533B Steel*," NUREG/CR-5142, U.S. Nuclear Regulatory Commission, Washington, DC (June 1988).
17. J.A. Joyce, D.A. Davis, E.M. Hackett, and R.A. Hays, "*Application of the J-Integral to Cases of Large Crack Extension*," NUREG/CR-5143, U.S. Nuclear Regulatory Commission, Washington, DC (February 1989).
18. J.A. Joyce and E. M. Hackett, "*Development of an Engineering Definition of the Extent of J Singularity Controlled Crack Growth*," NUREG/CR-5238, U.S. Nuclear Regulatory Commission, Washington, DC (May 1989).
19. J.A. Joyce and E.M. Hackett, "*Extension and Extrapolation of J-R Curves and Their Application to the Low Upper Shelf Toughness Issue*," NUREG/CR-5577, U.S. Nuclear Regulatory Commission, Washington, DC (March 1991).
20. J.A. Joyce, E.M. Hackett, and C. Roe, "*Comparison of J_{Ic} and J-R Curves for Short Crack and Tensile Loaded Specimen Geometries of a High Strength Structural Steel*," NUREG/CR-5879, U.S. Nuclear Regulatory Commission, Washington, DC (November 1992).
21. O'Dowd, N.P. and Shih, C.F., "*Two-Parameter Fracture Mechanics: Theory and Applications*," NUREG/CR-5958, U.S. Nuclear Regulatory Commission, Washington, DC (February 1993).
22. Kirk, M.T. and Dodds, R.H., Jr., "*J and CTOD Estimation Equations for Shallow Cracks in Single Edge Notch Bend Specimens*," NUREG/CR-5969, U.S. Nuclear Regulatory Commission, Washington, DC (July 1993).
23. Kirk, M.T. and Dodds, R.H., Jr., "*Approximate Techniques for Predicting Size Effects on Cleavage Fracture Toughness (J_c)*," NUREG/CR-5970, U.S. Nuclear Regulatory Commission, Washington, DC (July 1993).
24. Dodds, R.H., Jr., Shih, C.F., and Anderson, T.L., "*Continuum and Micromechanics Treatment of Constraint in Fracture*," NUREG/CR-5971, U.S. Nuclear Regulatory Commission, Washington, DC (July 1993).
25. Joyce, J.A. and Link, R.E., "*The Effect of Electric Discharge Machined Notches on the Fracture Toughness of Several Structural Alloys*," NUREG/CR-5981, U.S. Nuclear Regulatory Commission, Washington, DC (September 1993).
26. Joyce, J.A. and Link, R.E., "*Effects of Tensile Loading on Upper Shelf Fracture Toughness*," NUREG/CR-5981, U.S. Nuclear Regulatory Commission, Washington, D.C. (in press).
27. Dodds, R.H., Jr., Tang, M. and Anderson, T.L., "*Effects of Prior Ductile Tearing on Cleavage Fracture Toughness in the Transition Region*," NUREG/CR-6162, U.S. Nuclear Regulatory Commission, Washington, D.C. (in press).
28. Koppenhoefer, K.C., Dodds, R.H., Jr., and Kirk, M.T., "*Size and Deformation Limits to Maintain Constraint in K_{Ic} and J_c Testing of Bend Specimens*," NUREG/CR-6191, U.S. Nuclear Regulatory Commission, Washington, D.C. (in press).
29. Tang, M., Dodds, R.H., Jr., and Anderson, T.L., "*Effects of Ductile Crack Growth on Constraint Models for Cleavage Fracture*," NUREG/CR-6199, U.S. Nuclear Regulatory Commission, Washington, D.C. (in press).

Numerical Investigation of 3-D Constraint Effects on Brittle Fracture in SE(B) and C(T) Specimens

1. Introduction

Extensive plastic deformation often precedes fracture by transgranular cleavage in ferritic materials when tested in the low-to-mid range of the ductile-to-brittle transition (DBT) region (see [12,52,53,59] for examples). The interaction of crack-tip plastic zones with nearby traction-free surfaces and with global plastic zones affects strongly the near-tip stresses which control the onset of cleavage fracture. Stresses relax below the values determined uniquely by the J -integral [47] for the high constraint condition of small-scale yielding (SSY) [23] which exists early in the loading. This loss of a unique relationship between the crack-tip stresses and J , coupled with an *absolute* thickness effect due to random metallurgical variations and microstructural flaws along the crack front, underlies the specimen geometry, loading mode and size effect in tests to measure cleavage fracture toughness in the DBT region (see Wallin [59] for a review article). For example, shallow-crack SE(B)s with $a/W < 0.2$ frequently exhibit a factor of 3–5 elevation in fracture toughness relative to values measured for deep notch configurations having identical thickness [52,53]. Crack-tip plastic zones in SE(B)s with shallow cracks merge with the global bending plasticity on the tension surface of the specimen very early in the loading. A pronounced loss of crack-tip constraint follows which necessitates much larger J values to generate stresses sufficient to trigger cleavage.

In previous work by Dodds and Anderson [2,14], a local criterion for cleavage fracture was coupled with detailed, plane-strain finite element analyses to quantify the effects of planar dimensions and a/W ratio on toughness in SE(B) specimens. The research produced two key results for engineering applications: (1) recommended limits on measured *cleavage* toughness values (denoted J_c) for deep notch specimens to maintain near-tip stresses at SSY levels expressed by $b > MJ_c/\sigma_{flow}$ with $M = 200$ and σ_{flow} the average of yield and ultimate stresses; and (2) a “toughness scaling” procedure to correct measured J_c values for the loss of “in-plane” constraint due to large-scale yielding (LSY). Subsequent applications of this deformation/size limit and the toughness scaling model for a variety of steels tested with SE(B) and C(T) specimens indicate that [18,24,38,53,59,]: (1) the $M = 200$ limit is overly strict; studies of experimental data imply a limit of $M = 50$ – 100 for moderate to high hardening materials having power-law exponents of $n = 5$ – 10 ; and (2) the scaling model overcorrects for constraint loss in deep notch specimens at LSY for materials with lower amounts of strain hardening, $n \geq 10$.

These observations suggest the potential for a strong interaction between in-plane and through-thickness effects on crack-front fields not captured in the plane-strain analyses. Fully nonlinear, 3-D analyses of *through-crack* fracture specimens with refined meshes remain scarce due to the large-scale computational resources needed. Several studies (for example [13,26,32]) have provided quantitative descriptions of J variations along 3-D crack fronts; these analyses require only moderate mesh refinement to obtain satisfactory solutions. Brocks and Olschewski [8] were among the first to study the evolution of crack-front stresses under elastic-plastic conditions using 3-D models for deep notch specimens. Although the finite element meshes had less than a desired level of in-plane refinement, due to limits on computing resources, their results demonstrate the complex interaction of planar dimensions and thick-

† Numbers in [] indicate references listed in Section 7.

ness. Narasimhan, et al. [42] analyzed a plane-sided, thin SE(B) specimen having $W/B=8$ with a much more refined model and demonstrated the maintenance of high stress levels on the midplane at limit load.

Here we build upon these earlier efforts through systematic study of crack front fields for SE(B) and C(T) specimens obtained with very detailed, 3-D nonlinear analyses. By using 14 layers of elements over the half-thickness, and the same mesh refinement in each layer as employed in refined plane-strain analyses, these models capture fully the crack front stress fields over the loading history. Typical quarter-symmetric models have 7500 hexahedron elements. The analysis matrix for plane-sided specimens includes: SE(B)s having $a/W=0.1, 0.5, W/B=1, 2, 4$; C(T)s having $a/W=0.6, W/B=1, 2, 4$; with strain hardening exponents of $n=5, 10$ and 20 for each configuration. For an $n=10$ material, we examine the effects of 20% side grooves (10% each side) by analyzing a C(T) having $a/W=0.6, W/B=2$ and SE(B)s having $a/W=0.1, 0.5, W/B=2$.

We characterize the crack front fields obtained from these 3-D analyses using the J - Q [44,45] and toughness scaling methodologies to quantify constraint effects. The 3-D analyses reveal much greater through-thickness variations in crack front stresses for deep notch specimens than for shallow-notch specimens. Stress triaxiality on the specimen midplane of deep notch specimens remains at SSY levels to higher (local) J values than indicated by the plane-strain models. Crack front stresses near the outside surfaces of plane-sided specimens fall well below midplane levels and well below plane-strain levels. The maintenance of SSY conditions over a substantial part of the specimen thickness to higher J -levels than found in the plane-strain analyses indicates that the $M=200$ limit on measured J_c values for deep notch specimens may be relaxed to $M \approx 75-100$ for moderate hardening, which brings the analytically determined value into closer accord with experimental observations. For shallow-notch SE(B)s with $W/B=1, 2$, the plane-strain analyses provide remarkably good descriptions of stresses ahead of the crack tip; this perhaps explains the surprisingly good J - Q correlations and toughness constraint corrections for such specimens.

Finally, we propose an extension of the toughness scaling methodology applicable for cleavage fracture in the DBT regime which: (1) replaces the plane-strain constraint corrections with the new, 3-D "in-plane" constraint corrections at locations along the crack front and (2) includes the *absolute* thickness effect predicted by extreme value statistics on fracture toughness, with the actual thickness B replaced by an "effective" thickness, B_{eff} . When the stress field varies along the crack front, B_{eff} defines that portion of thickness over which stresses increase to cleavage triggering levels. For non-side grooved SE(B)s, values of B_{eff}/B lie in the range of 0.4-0.8 with a dependence on the $a/W, W/B$ ratios and material flow properties. Perhaps surprisingly for specimens with side grooves, B_{eff}/B exceeds slightly the value for the corresponding plane-sided specimen even though the front length decreases by 20%. The extensive numerical analyses performed here provide a representative set of solutions to support this approach for interpretation of experimentally measured J_c values.

2. Descriptions of Constraint and Statistical Effects

Innovative approaches have evolved over the past five years to quantify constraint and to describe the effects of constraint variations on macroscopic (engineering) fracture toughness characterized by J , or equivalently the crack tip opening displacement, CTOD (δ). We consider two related lines of investigation: (1) extensions of traditional fracture mechanics which employ J and a scalar (triaxiality) parameter to describe the elastic-plastic, near-tip fields;

fracture toughness for a material takes the form of an experimentally measured *toughness locus* expressed by J and the second parameter, and (2) models motivated by the specific micro-mechanism of transgranular cleavage; often referred to as *local* approaches, these models predict the toughness locus from the experimental results for a small number of key fracture tests. A complete model representative of this second approach requires treatment of absolute thickness effects caused by random metallurgical variations—microstructural flaws along the crack front; most often extreme value statistics are adopted for this purpose.

The most widely cited examples of the first approach include, in order of increasing generality: (a) the higher-order, asymptotic expansion of crack-tip fields as developed by Chao et al. [10,64] following earlier work of Li and Wang [30] and Sharma and Aravas [49], (b) the J - T methodology developed by Hancock and co-workers [1,6,16], Parks and co-workers [41,60,61,62] building upon earlier work by Bilby, et al. [7] and Leever and Radon [28], and (c) the J - Q methodology developed by O'Dowd and Shih [44,45]. Parks [46] provides a critical review and assessment of these methodologies. In each one, the J -integral sets the size scale over which large deformations and high stresses develop while the additional parameter(s) quantifies the level of stress triaxiality at distances of a few CTODs ahead of the tip. Under increased loading, each fracture specimen follows a characteristic driving force curve, or trajectory, which defines the evolution of crack-tip deformation (J) and constraint (T , Q , amplitudes of terms in asymptotic expansion). Lines connecting the measured fracture points on these trajectories for specimens tested with varying constraint levels define the toughness locus for the material.

These extensions to the traditional "correlative parameter" form of fracture mechanics become impractical as the number of specimens required to define the toughness locus increases and as the range of temperatures increases (each temperature may require a different toughness locus, for example in the DBT region). The second approach offers the potential to alleviate this difficulty through a fracture criterion expressed in terms of the near tip strains-stresses and the values of critical, microscale material properties. For a fixed set of microscale properties, conventional finite element analyses of fracture specimens enable development of correlations between macroscopic values of fracture driving force (J) and critical combinations of near-tip strains-stresses which satisfy the local fracture criterion. By analyzing various geometries, crack sizes and loading modes (tension *vs.* bending), points on the toughness locus may be predicted.

Early developments in this direction for cleavage fracture include the works of Batdorf and Crose [4] and Evans [17] (which postulated a modified Weibull theory for brittle fracture under multiaxial stress states) and the critical stress-critical distance model of Ritchie et al. [48] and Curry and Knott [11]. Subsequent investigators addressed the pronounced effects of microscopic material variability on the scatter of macroscopic fracture toughness. Key contributions toward the current treatment of macroscopic scatter focus on weakest link models. The Beremin group [5] first introduced the Weibull stress as a fracture parameter. Mudry extended the approach with plane-strain finite element analyses to include large-scale yielding effects on the Weibull stress; size/deformation limits for fracture testing followed from deviation of the specimen Weibull stress from small-scale yielding values (refer to comprehensive article by Mudry [39]). Wallin [55,54] followed with construction of a more general weakest link model and later included the statistical effects of specimen thickness [56], an approximate correction for small amounts of ductile crack extension [57] and discussion constraint loss effects on cleavage fracture toughness [58,59]. Brückner-Foit, et al. [9] concluded from

partially successful attempts at experimental validation that coupling of thickness and in-plane effects on the crack front stresses plays a key role in the applications of the weakest link approach. Minami, Bruckner-Foit et al. [35] included these effects to predict the toughness distributions across different specimen geometries. Paralleling these more recent efforts, Dodds and Anderson [14,2] proposed the so-called "toughness scaling" methodology which provides a direct means to assess the effects of constraint loss on cleavage fracture toughness (J_c) without explicit reference to a statistical argument or a triaxiality parameter. Numerous *local*-type approaches for initiation of ductile tearing (J_{Ic}) and *R*-curve behavior have been proposed; however, they are not germane to the present discussion of cleavage fracture in the DBT region.

To examine 3-D effects on SE(B) and C(T) specimens in the present work, we adopt the *J-Q* methodology from the first approach and the toughness scaling methodology from the second approach. The following sections outline very briefly the central points of each methodology; Dodds, et al. [15] provide more complete descriptions. We then outline a proposed extension of the toughness scaling methodology for 3-D configurations which incorporates both constraint loss and statistical effects on cleavage fracture.

2.1 *J-Q* Theory

The *J-Q* description of Mode-I, plane-strain crack tip fields derives initially from consideration of the boundary layer model for small-scale yielding (SSY). Crack-tip stresses for linear elastic conditions have the form [63]

$$\sigma_{ij} = \frac{K_I}{\sqrt{2\pi r}} f_{ij}(\theta) + T\delta_{1i}\delta_{1j} \quad (1)$$

Here r and θ are polar coordinates centered at the crack tip with $\theta = 0$ corresponding to a line ahead of the crack and $K_I = \sqrt{EJ/(1-\nu^2)}$ where J denotes Rice's *J*-integral [47], E is Young's modulus and ν is Poisson's ratio. Crack tip fields differing in stress triaxiality are generated by varying the non-singular stress, T , parallel to the crack plane (which does not affect the value of J). In the computational model for SSY, the conditions defined by Eq (1) are imposed incrementally on the remote outer boundary of a symmetrically constrained, semi-circular mesh of elements focused on the crack tip.

O'Dowd and Shih [44,45] employed asymptotic analyses and detailed finite element analyses to propose the approximate two-parameter description of the crack tip fields which applies under small and large-scale yielding conditions

$$\sigma_{ij} = \sigma_0 f_{ij}\left(\frac{r}{J/\sigma_0}, \theta; Q\right), \quad \varepsilon_{ij} = \varepsilon_0 g_{ij}\left(\frac{r}{J/\sigma_0}, \theta; Q\right) \quad (2)$$

The dimensionless second parameter, Q , in Eq. (2) defines the amount by which σ_{ij} and ε_{ij} in fracture specimens differ from the adopted $SSY_{T=Q=0}$ reference solution at the same applied- J . For non-zero values of the T -stress, Q exhibits a simple (unique) dependence on T in SSY that varies only with the material flow properties [45].

To a good approximation, O'Dowd and Shih showed that $Q\sigma_0$ represents the *difference* in hydrostatic stress over the forward sector ahead of the crack tip between the $SSY_{T=0}$ and fracture specimen fields, i.e.,

$$\sigma_{ij} = (\sigma_{ij})_{SSY;T=0} + Q\sigma_0\delta_{1i}\delta_{1j}; \quad |\theta| < \frac{\pi}{2}, \quad J/\sigma_0 < r < 5J/\sigma_0 \quad (3)$$

Operationally, Q is defined by

$$Q \equiv \frac{\sigma_{\theta\theta} - (\sigma_{\theta\theta})_{SSY;T=0}}{\sigma_0}, \quad \text{at } \theta = 0, r = 2J/\sigma_0 \quad (4)$$

where the specimen stresses ($\sigma_{\theta\theta}$) in Eq (4) are evaluated from finite element analyses containing sufficient mesh refinement to resolve the fields at this length scale (where the fracture specimen and SSY are loaded to the same J). No restrictions are imposed on material flow properties, e.g., a Ramberg–Osgood representation. Large geometry changes may be included although values of Q derived from small geometry change analyses prove satisfactory in applications which make use of stresses outside the near–tip blunting region.

At low deformation levels, fracture specimens experience SSY conditions and Q remains very nearly zero (Q and T are uniquely related under SSY, and T varies linearly with K_I). Once large–scale yielding conditions prevail, hydrostatic stresses at the crack tip are substantially less than those in $SSY_{T=0}$ at the same J –value. This difference produces *negative* Q values once the specimen deviates from SSY conditions. For deeply notched SE(B) and C(T) specimens, the elastic T –stress is positive and thus Q takes on slightly positive values at low deformation levels before constraint loss occurs.

For 3–D, Mode–I configurations, we argue that near–tip fields at locations sufficiently far from external surfaces approach the form of Eq. (2) as $r \rightarrow 0$. The use of Eq. (4) provides Q values at locations (x_3) along a 3–D crack front using local J –values and stresses in planes perpendicular to the crack front. Alternatively, the direct interpretation of Q as the hydrostatic (mean) stress suggests a definition in 3–D as

$$Q_m \equiv \frac{\sigma_{kk} - (\sigma_{kk})_{SSY;T=0}}{\sigma_0}, \quad \text{at } \theta = 0, r = 2J/\sigma_0 \quad (5)$$

Previous studies by Dodds, et al. [15] demonstrate the negligible differences between Q and Q_m for through–crack and surface crack configurations.

2.2 Toughness Scaling Model for Cleavage

Dodds and Anderson [2,14] quantify constraint effects on fracture toughness by coupling the global fracture parameter (J_c) with a near–tip failure criterion applicable to transgranular cleavage. They adopt the material volume ahead of the crack front over which the normalized (maximum tensile) principal stress, σ_1/σ_0 , exceeds a critical value, $\bar{\sigma}_c$, as the local failure criterion. For the same material/temperature combination, attainment of equivalent stressed volumes ahead of the crack front in different specimens implies the same *probability* for triggering cleavage fracture. This model leads immediately to a weakest–link interpretation but a more general interpretation as a stress–controlled mechanism seems plausible. The “toughness scaling” aspects of the model arise from its often expressed form of (see [15])

$$J_{FB}/J_0 = \sqrt{A_0(\bar{\sigma}_c)/A_{FB}(\bar{\sigma}_c)} \quad (6)$$

where A_0 denotes the area enclosed within the principal stress contour $\sigma_1/\sigma_0 = \bar{\sigma}_c$ for an applied $J = J_0$ in the $SSY_{T=0}$ boundary layer model (plane–strain, unit thickness). A_{FB} denotes the enclosed area for the same contour in a (plane–strain, unit thickness) fracture specimen loaded to $J = J_{FB}$. In applications, J_{FB} takes on the measured value at fracture, J_c , with A_{FB} estimated from finite element analyses or the J – Q description of the near–tip stresses. Cata-

logged solutions for $SSY_{T=0}$ using the material flow properties provide the unique ratio $A_0\sigma_0^2\epsilon_0^2/J_0^2$ for each value of $\bar{\sigma}_c$. By setting $A_0 \equiv A_{FB}$ in this expression, J_0 is found and used to compute the scaling ratio J_{FB}/J_0 for each loading level and for a range of principal stress values. The ratio quantifies the effects of "in-plane" constraint variations on cleavage fracture toughness. A critical value of J_0 represents the fracture toughness of an infinitely large specimen ($SSY_{T=0}$); $J_{FB}/J_0 > 1$ implies that the specimen has experienced a constraint loss that causes the commonly observed increase in measured fractured toughness.

Computational studies of SSY with $T \neq 0$ and of various fracture specimens often reveal a noticeable independence of the J_{FB}/J_0 ratio on the selected $\bar{\sigma}_c$ (which must be sufficiently large, e.g., > 2 , so that the contour lies entirely in the forward sector and in the plastic zone). The J - Q description of the principal stresses implies that the shape of principal stress contours is maintained while the relative magnitude of the contours varies directly with the hydrostatic stress $Q\sigma_0$. This similarity of principal stress contours prevails only to the extent that the approximate J - Q description of the crack tip stresses remains valid. At very large-scale yielding, particularly for specimens subjected to severe global bending, the similarity breaks down and J_{FB}/J_0 varies strongly with $\bar{\sigma}_c$.

2.3 Extensions for 3-D Configurations Including Statistical Effects

Experimental results and metallurgical models for cleavage in ferritic steels demonstrate an *absolute* thickness effect on fracture toughness not related to constraint [43]. Metallurgical variations in the material and the random incidence of microstructural flaws along the crack front require a statistical treatment of thickness in experimental fracture toughness data. Wallin [54,59] employs extreme value statistics to derive a three-parameter Weibull correction for fracture toughness data in specimens having a common a/W but different thickness ($B_{(1)}$ and $B_{(2)}$) which fail by cleavage without previous ductile tearing,

$$K_{Ic-(2)} = K_{min} + (K_{Ic-(1)} - K_{min}) \sqrt[4]{B_{(1)}/B_{(2)}} \quad (7)$$

where K_{min} denotes the threshold toughness of the material for an infinitely long crack front. Recasting Eq (7) in terms of J yields,

$$J_{c-(2)} \approx J_{c-(1)} \sqrt{B_{(1)}/B_{(2)}} \quad (8)$$

where the J equivalent of K_{min} has been neglected as a small term; it has little effect on the cumulative Weibull distribution. The development of Eqs. (7,8) assumes that each point along the crack front experiences the same local J -value and corresponding SSY stress field. Consequently, the correction reflects different volumes of material sampled along the crack front due only to thickness differences. Because the failure of a weak metallurgical defect controls cleavage fracture, fracture toughness decreases with increasing probability (thickness) of finding a defect.

In common fracture specimens, however, J and the near-tip stresses vary (often strongly) along the crack front under increased loading, with stresses decreasing below SSY values due to constraint loss. Specimen thickness, planar dimensions, crack size and material flow properties interact in a complex manner under increasing plastic deformation to govern the intensity of crack front stresses. Consequently, straightforward applications of Eqs. (7,8) beyond proportionally sized specimens appear reasonable only for restricted combinations of low deformation, large specimens and moderate-to-strong strain hardening.

Motivated by the above discussion, we propose a 3-D form of the toughness scaling model which reflects both the statistical effects of volume sampling due to thickness differences and the constraint loss on crack-front stress fields due to large-scale yielding. At a given loading level (J), consider a specific principal stress contour, $\sigma_1/\sigma_0 = \bar{\sigma}_c$, that encloses the tip at each location along the crack front. Let $A(s, \bar{\sigma}_c)$ denote the area enclosed by the contour which lies in the principal normal plane to the crack front at location s along the front. At location $s = s_{max}$, the enclosed area attains a maximum value $A_{max} \equiv A(s_{max}, \bar{\sigma}_c)$. The volume of material along the crack front over which the principal stress exceeds $\bar{\sigma}_c$ is given by (for a straight crack front)

$$V(\bar{\sigma}_c) = \int_{-B/2}^{B/2} A(s, \bar{\sigma}_c) ds \quad . \quad (9)$$

We suggest replacing the actual specimen thicknesses appearing in Eq. (8) with effective thicknesses, $B_{eff} = V/A_{max}$, which quantify the actual portion of specimen thicknesses over which crack-front stresses reach levels sufficient to trigger cleavage. As shown in a later section, A_{max} occurs on the midplane of SE(B) and C(T) specimens except a shallow crack, SE(B) with $B = W$. Moreover, the front location at which A_{max} occurs has the maximum "in-plane" constraint, and the ratio B_{eff}/B defines the equivalent fraction of the specimen thickness subjected to that constraint level. We show that B_{eff}/B decreases from near unity under linear elastic conditions, for plane-sided specimens, to a nearly deformation independent value once large-scale yielding conditions prevail. Moreover, B_{eff}/B remains reasonably insensitive to a range of realistic $\bar{\sigma}_c$ values. The B_{eff}/B ratio varies significantly with W/B for fixed a/W and material strain-hardening characteristics; the ratio decreases with increasing W/B while greater amounts of strain hardening elevate values of B_{eff}/B . Still other analyses examine the effects of side grooves on B_{eff}/B in C(T) and SE(B) specimens.

To accommodate the potentially strong influence of constraint loss from "in-plane" effects, we suggest replacing $J_{c-(1)}$ in Eq. (8) with $J_0(J_{c-(1)})$, where computation of J_0 follows the 2-D model of Eq. (6) with $A_{FB} \equiv A_{max}$. A measured toughness value, J_c , is then constraint and thickness corrected to a SSY condition with a convenient reference thickness ($B = B_{ref}$) using the modified form of Eq. (8)

$$\bar{J}_0 = J_0(J_c) \sqrt{B_{eff}/B_{ref}} \quad . \quad (10)$$

The quantity B_{ref} may be assigned a convenient value of 25 mm for SI units or 1 in. for English units. The corrected set of \bar{J}_0 values from different specimens are then given equal weight in further statistical treatments of toughness values to define, for example, confidence bounds. Key features of the model include the reasonably strong independence of B_{eff}/B and $J_0(J_c)$ on the selected $\bar{\sigma}_c$ for low constraint specimen configurations in most need of the correction. In deep notch SE(B)s and C(T)s, SSY conditions often exist on the midplane at fracture and only the effective thickness correction is required. For these specimens, B_{eff}/B remains reasonably independent of $\bar{\sigma}_c$. Finally, given a value of \bar{J}_0 for the material, the corresponding J_c -value for a specific fracture specimen may be computed using the reverse of the process described above; the B_{eff}/B and $J_0(J_c)$ corrections must be known for the fracture specimen. In principle, the concept of B_{eff} can be extended to correlate surface crack and through-crack configurations although the finite element modeling and post-processing require considerable effort to evaluate the integral in Eq. (9) for the surface crack geometry.

3. Computational Procedures

3.1 3-D Finite Element Models

Figure 1 shows typical finite element models constructed for the 3-D analyses of SE(B) and C(T) specimens. Reflective symmetry about the crack plane ($x_2 = 0$) and the longitudinal mid-plane ($x_3 = 0$) enable the use of one-quarter models as indicated. Each model has a straight crack front defined along $x_1 = x_2 = 0$, $0 \leq x_3 \leq B/2$. The meshes consist of 8-node, hexahedron isoparametric elements arranged into 14 variable thickness, planar layers; the thickest layer being defined at $x_3 = 0$ with much thinner layers defined near the free surface ($x_3 = B/2$) to accommodate strong x_3 variations of the field quantities. Within each layer, 40 focused rings of elements enclose the crack front. The size of each ring increases gradually with radial distance (r) from the crack front, where $r = (x_1^2 + x_2^2)^{1/2}$. In the angular direction, $\theta = \tan^{-1}(x_2/x_1)$, 4 equal sized elements are defined over $0 \leq \theta \leq \pi/4$ with 6 equal sized elements defined over $\pi/4 \leq \theta \leq \pi$. The innermost ring of elements incident on the crack front contains 8-node hexahedrons collapsed into wedges with initially coincident nodes along the crack front left unconstrained to permit blunting deformations. In each layer, these models provide a level of mesh refinement comparable to those constructed for previous plane strain analyses (see, for example, [1,14,44,45]). Typical 3-D models for the SE(B) and C(T) specimens contain 6500–8500 elements.

The analysis matrix includes plane-sided SE(B) specimens with $a/W=0.1$ and 0.5 , $W/B=1, 2, 4$ and plane-sided C(T) specimens with $a/W=0.6$, $W/B=1, 2, 4$. To investigate the potential effects of 20% side grooves (10% each side) on standard $W/B=2$ configurations, we analyze three specimens: a C(T) having $a/W=0.6$ and SE(B)s having $a/W=0.1$ and 0.5 . As indicated in Fig. 1(b), side grooves are introduced by releasing the x_2 constraints on the affected crack-plane nodes and then translating nodes in the outermost 4 layers of elements by required distances in the x_2 direction; the notch radius of the side groove is not modelled.

These 3-D models represent a compromise between the required level of mesh refinement to resolve the in-plane and through-thickness gradients of the stress fields and the extensive computation (CPU) times required for each analysis. Convergence studies with fewer elements in the thickness (x_3) direction yielded unsatisfactory results as did analyses with fewer elements over the depth (W) in the SE(B) specimens. The reduced angular increment of element size over $0 \leq \theta \leq \pi/4$ also reflects the outcome of preliminary analyses which revealed insufficient resolution of the principal stress contours in the $x_1 - x_2$ plane.

3.2 Constitutive Model

The material model employs deformation plasticity theory (J_2 nonlinear elasticity) in a conventional small geometry change (SGC) setting. The SGC and large geometry change (LGC) assumptions provide consistent descriptions of the crack front stress fields at distances outside the finitely deformed, blunting zone having a peak stress at $r \approx J/\sigma_0$ [33,50]; cleavage fractures most often originate over distances at or beyond the peak stress location predicted by the LGC analyses [19,34].

The uniaxial (tension) stress-strain curve follows a linear then power-law model given by

$$\frac{\epsilon}{\epsilon_0} = \frac{\sigma}{\sigma_0} \quad \epsilon \leq \epsilon_0 ; \quad \frac{\epsilon}{\epsilon_0} = \left(\frac{\sigma}{\sigma_0} \right)^n \quad \epsilon > \epsilon_0 \quad (11)$$

where ϵ_0 and σ_0 define limits for the initial linear portion of the response. A small transition region eliminates the discontinuous tangent modulus at $\epsilon = \epsilon_0$; nonlinearity of the $\sigma - \epsilon$ curve actually begins at $\epsilon = 0.95\epsilon_0$. The transition region significantly enhances the convergence rate of the global Newton iterations. Wang [62] provides additional details of this constitutive model. Computational results are presented for a strongly hardening material ($n = 5$) characteristic of civil and marine structural steels, for a moderately hardening material ($n = 10$) characteristic of many pressure vessel and pipeline steels and for a very low hardening material ($n = 20$). All computations use $E/\sigma_0 = 500$ and Poisson's ratio $\nu = 0.3$.

3.3 Solution Procedures

Finite element results were generated with the vectorized research code WARP3D [27] which employs an incrementally-iterative Newton procedure to resolve the nonlinear equilibrium equations. The code solves the linearized equilibrium equations at each iteration with an efficient implementation of the element-by-element, linear pre-conditioned conjugate gradient (LPCG) method which eliminates assembly of the large tangent-stiffness matrix [21,22]. The code architecture based on the LPCG solver reduces both solution runtimes and real memory requirements significantly below those for conventional codes using direct solvers.

Figure 1 indicates the loading arrangement for the SE(B) and C(T) models. A typical analysis uses 25-30 load increments to generate the complete response with 3-4 Newton iterations for convergence within each step to a tight tolerance on residual nodal forces. Numerical results were generated on Cray-90 and Convex supercomputers. A 9300 node, 7700 element model requires 40-70 seconds of CPU time for solution of a load increment on the Cray-90 using a single processor.

The conventional 8-node, hexahedron element exhibits severe volumetric locking under incompressible plastic deformation. The WARP3D code adopts the $\bar{\mathbf{B}}$ modification suggested by Hughes [20] to alleviate the locking behavior. Volumetric terms of the strain-displacement relationship at each of the $2 \times 2 \times 2$ Gauss points are replaced with a "mean-dilatation" set of volumetric terms which yields a uniform mean stress over the element (Nagtegaal, et al. [40]).

The local energy release rate for Mode I crack extension at each point s along the front is given by [36,37]

$$J_{local}(s) = \lim_{\Gamma \rightarrow 0} \int_{\Gamma} \left[\mathcal{W} n_1 - \sigma_{ij} \frac{\partial u_i}{\partial x_1} n_j \right] d\Gamma \quad (12)$$

where \mathcal{W} denotes the strain-energy density, Γ is a vanishingly small contour in the principal normal plane at s , n is a unit normal vector to Γ , σ_{ij} and u_i are Cartesian components of stress in the crack front coordinate system. For two-dimensional configurations modelled with a nonlinear elastic material, the above expression simplifies to the conventional J -integral for Mode I [47]. In the present analyses, numerical evaluation of Eq. (12) is accomplished with a domain integral method [29,51] as implemented in WARP3D. The resulting formulation provides pointwise values of J across the crack front and the thickness-average value (J_{avg}) at each loading level. As shown in the next section, the thickness average values agree very well with J -values computed from the finite element load-displacement curves using a conventional energy separation procedure.

3.4 SSY Boundary Layer Models

The SSY reference fields required for Q and J_{FB}/J_0 computations are obtained from plane-strain, finite element solutions of the modified boundary layer model of an infinite body, single-ended crack problem [1,23]. Displacements u_i of the elastic, Mode I field are applied to the outer boundary of a semi-circular region containing an edge crack as illustrated in Fig. 2(b)

$$u(r, \theta) = K_I \frac{1-\nu}{E} \sqrt{\frac{r}{2\pi}} \cos\left(\frac{\theta}{2}\right) (3 - 4\nu - \cos\theta) + T \frac{1-\nu^2}{E} r \cos\theta \quad (13)$$

$$v(r, \theta) = K_I \frac{1-\nu}{E} \sqrt{\frac{r}{2\pi}} \sin\left(\frac{\theta}{2}\right) (3 - 4\nu - \cos\theta) - T \frac{\nu(1+\nu)}{E} r \sin\theta \quad (14)$$

where r is the radial distance from the crack tip, $K_I = \sqrt{EJ_0/(1-\nu^2)}$ and T is the stress parallel to the crack. K_I and T alone control the stress state in the near vicinity of the crack tip under SSY conditions. For consistency with the J - Q methodology, we choose the highly constrained, $T=0$ configuration for the reference field.

Figure 2(a) shows the opening mode stresses on the crack plane. For convenience in post-processing the 3-D finite element solutions, continuous functions are constructed to fit the SSY stresses which take the form

$$\frac{\sigma_{\theta\theta}}{\sigma_0} = \alpha \hat{r}^\beta \exp(\gamma \hat{r}); \quad \hat{r} = \frac{r}{J/\sigma_0 \varepsilon_0} \quad (15)$$

and α, β, γ are curve fitting parameters. The table included in Fig. 2(a) lists the values of these parameters for $n=5, 10$ and 20 . These fits apply for all E/σ_0 ratios (recall that the similarity length-scale of the HRR fields is \hat{r} as defined above). Figure 2(b) shows the corresponding areas within a range of principal stress contours enclosing the crack tip. Again, continuous functions are constructed to fit the SSY contour areas which have the form

$$\bar{A} = \log_{10} \left(\frac{A_0 \sigma_0^2 \varepsilon_0^2}{J_0^2} \right) = H_0 + H_1 \left(\frac{\sigma_1}{\sigma_0} \right) + H_2 \left(\frac{\sigma_1}{\sigma_0} \right)^2 + H_3 \left(\frac{\sigma_1}{\sigma_0} \right)^3 + H_4 \left(\frac{\sigma_1}{\sigma_0} \right)^4 \quad (16)$$

The table included in Fig. 2(b) lists the values of the fit parameters $H_0 \rightarrow H_4$ for $n=5, 10$ and 20 . By including ε_0^2 in the normalizations of Eqs. (15,16) as indicated, the fits apply for all E/σ_0 ratios (this is readily verified by integrating the area enclosed within the maximum principal stress contour as defined by the HRR field).

4. Results and Discussion

The following sections provide selected key results of the extensive numerical analyses conducted on the SE(B) and C(T) specimens. Where possible, tables of numerical values summarize the complete range of cases modeled ($n=20$ results are included in tables but not in graphs). The presentation begins with descriptions of conventional fracture driving force measures, J and CTOD, including new values for the non-dimensional η_{pl} factors needed to compute J from measured experimental quantities. Constraint variations in planes perpendicular to the crack front are then characterized in terms of J - Q trajectories and the toughness scaling model. The section concludes with development and study of the B_{eff}/B ratios required for application of the proposed 3-D toughness scaling model.

4.1 Global Response: J and CTOD Distributions Over the Crack Front

Figure 3(a) shows the computed load-crack mouth opening displacement (CMOD) relationships for three W/B ratios of the deep notch SE(B) geometry ($n=10$). The figure also includes

the corresponding plane-strain solution for reference and the 3-D solution for a specimen with $W/B = 2$ having 20% side grooves. Not surprisingly, the $W/B = 1$ configuration most closely matches the plane-strain response. With the full thickness B used for load normalization, the response for the side groove specimen falls just below that for the $W/B = 2$ plane-sided specimen. We found identical load-CMOD trends for the deep notch SE(B) with $n = 5$ and a somewhat smaller effect of the W/B ratio on the response for the shallow notch SE(B) specimen ($a/W = 0.1$).

Experimentalists most often estimate J -values using the expression (see Chp. 7 of [3])

$$J = J_{el} + J_{pl} = \frac{K_I^2(1 - \nu^2)}{E} + \eta_{pl} \frac{U_{pl}}{bB} \quad (17)$$

where J_{el} and J_{pl} denote the elastic and plastic contributions to J and U_{pl} defines the (unrecoverable) plastic work of the applied load. The non-dimensional plastic "eta" factor, η_{pl} , describes the effect of plastic work normalized by the ligament area on the applied J . For deep notch SE(B)s, testing standards prescribe a value of 2.0 for η_{pl} . Kirk and Dodds [25] generated an extensive set of η_{pl} values using plane-strain analyses of SE(B) specimens for a wide range of a/W ratios and hardening properties. For $a/W < 0.2$, they find η_{pl} to be much less sensitive to the hardening properties when U_{pl} is computed from CMOD rather than load-line displacement.

Table 1 summarizes a comprehensive set of η_{pl} values derived from the present 3-D analyses of SE(B) and C(T) specimens including the side-groove models. Figure 3(b) illustrates the computational procedure to compute the η_{pl} values. At each load increment, the domain integral computations produce a thickness average J -value and a J -value at selected locations across the crack front. Using K_I computed from a 3-D elastic analysis of the specimen, the J_{el} term is computed as defined in Eq. (17) and then subtracted from domain integral J -values leaving J_{pl} . The plastic work term, U_{pl} , at each load increment follows from direct evaluation of plastic work done by the applied loads acting through the nodal displacements. The J_{pl} and U_{pl} terms are normalized and plotted as shown in Fig. 3(b). The strong linear relationship present in Fig. 3(b) holds across all configurations and hardening properties. Linear regression then yields the η_{avg} value to compute the thickness average J and the η_{max} value to compute the maximum J -value over the crack front. Table 1 includes η_{pl} values for U_{pl} based on plastic load-line displacement (Δ_{LLD-pl}) and on plastic CMOD ($\Delta_{CMOD-pl}$); Δ_{LLD-pl} taken from the finite element solution corresponds to the value measured by a comparator bar apparatus. In deep notch SE(B) and C(T) specimens, η_{pl} values for the thickness average J agree well with those found in the earlier plane-strain analyses and with those currently prescribed in testing standards; a minimal effect of strain hardening is observed. The 3-D η_{pl} values based on Δ_{LLD-pl} for shallow notch SE(B)s again reveal ≈ 20 – 25% variation over the hardening range $n = 5 \rightarrow 20$, while the η_{pl} values based on $\Delta_{CMOD-pl}$ show only ≈ 4 – 5% variation.

Figures 4 and 5 show the distributions of J over the crack front under increasing load levels for selected configurations, with values at each front location normalized by J at the midplane. The thickness average value, denoted J_{avg} , describes the load level for each curve. The deformation levels range from SSY to beyond plastic hinge formation. Figures 4 (a,b) show the front distributions for the shallow notch SE(B) with $W/B = 2$ and two hardening levels ($n = 5, 10$). The maximum J occurs at the midplane, with a gradual transition from the nearly uniform front response in SSY to an essentially constant, relative distribution once a plastic hinge forms. Increased strain hardening promotes a slightly more uniform front distribution. The distributions for all deep notch, plane-sided SE(B) specimens follow those shown in Figs. 4

(a,b). The J distributions for the shallow notch with $W/B = 1$, shown in Figs. 4 (c,d), differ from all other plane-sided configurations analyzed; the maximum J occurs not at the midplane but nearer the outside surface. Koers et al. [26] report a similar J distribution which is attributed to anticlastic bending effects not present in configurations with larger aspect ratios. The η_{pl} values in Table 1 (η_{max}) to compute a maximum front J for this configuration refer to the $x_3/(B/2) = 0.53$ location. As shown in the next section, this location on the front maintains the highest constraint level.

Figure 5 shows distributions of J across the crack front for a plane-sided and a 20% side-grooved C(T) specimen. The plane-sided distribution follows closely those for the deep notch SE(B) specimens. For the side-grooved specimen, the distributions at SSY load levels peak near the the root of the side groove; at LSY levels, the distribution becomes nearly uniform over the front. DeLorenzi and Shih [13] report crack front distributions obtained with coarse models which exhibit very similar trends to those shown here.

Typical distributions of CTOD values, as defined by the 45° intercept method, are shown in Fig. 6 for the deep and shallow notch SE(B) specimens. The deep notch CTOD distributions follow the same trend as the J distributions with peak values at the center and values $\approx 50\%$ lower near the outside surface. For the shallow notch specimens, peak CTOD values occur at midplane under SSY conditions and at the outside surface under LSY conditions. This same trend is observed for $W/B = 1, 2$, and 4 for all hardening exponents with largest outside to midplane ratio for $n = 5$, $W/B = 1$. The falling J -values coupled with increasing CTOD values at the outside surface imply a very low m -factor in the relation $J_{local} = m\sigma_{flow}\delta_{local}$. Table 2 summarizes the m -factors obtained from the 3-D analyses. These m -factors describe the relationship between the *local* CTOD and *local* J -values at the midplane location of the crack front except for the SE(B)s having $a/W = 0.1$, $W/B = 1$; for these specimens, m -factors are given for the midplane and $x_3/(B/2) = 0.53$ locations.

4.2 Crack Front Stress Triaxiality: J - Q Trajectories

Figures 7-9 provide descriptions of crack front constraint in terms of J - Q trajectories. Figures 7 (a) and (b) show the J - Q trajectories generated under increased loading at locations over the crack front for plane-sided, deep and shallow notch SE(B) specimens having $W/B = 1$ and $n = 10$. In these figures, Q is defined by Eq. (4) at the normalized distance ahead of the crack front given by $r/(J_{local}/\sigma_0) = 2$. However, we plot the evolution of Q values against specimen deformation described by J_{avg} rather than J_{local} , where J_{avg} represents the value that would be reported from experimental work using a plastic η -factor. For the deep notch in Fig. 7(a), Q -values are positive at low loads (corresponding to the positive elastic T -stress for this geometry) except near the outside surface. Over the center portion of the specimen thickness, SSY conditions ($Q \geq 0$) exist *strictly* for deformation levels $b > 140J_{avg}/\sigma_0$, where b denotes the remaining ligament length; at larger deformations Q takes on negative values. The plane-strain result for this configuration shown in Fig. 7(a) indicates constraint loss at lower-levels of deformation, $b > 170J/\sigma_0$. Q -values at various distances ahead of the tip on the midplane, see Fig. 7(c), show steadily increasing radial dependence under increasing load which reflects the strong gradient of the bending field acting on the small remaining ligament. All deep notch SE(B) and the C(T) specimens exhibit similar levels of Q dependence on r at large deformations.

In Fig. 7(b), Q -values for the $a/W = 0.1$ configuration reveal an immediate loss of constraint upon loading. Crack front locations maintaining highest constraint are $x_3/(B/2) \sim 0.3-0.68$ rather than at the midplane for all other configurations examined. Strong anticlastic bending

in the square cross-section contributes to this different behavior. The plane-strain result agrees reasonably well with the 3-D analysis over this portion of the crack front. Fig 7(d) demonstrates the much stronger radial independence of Q -values for the $a/W = 0.1$ configuration. The global bending field impinges less strongly on the crack-tip fields in the shallow notch geometry. However, no practical size/deformation limit exists to maintain SSY conditions in this specimen; constraint loss occurs upon initial loading.

Figure 8 provides additional J - Q trajectories for SE(B) specimens showing the effects of W/B and a/W ratios, strain hardening and side grooves. In each case, the trajectories are shown for the crack front location having maximum constraint (least negative Q values) with Q given by Eq. (4). This location corresponds to the midplane in all configurations except $a/W = 0.1$, $W/B = 1$. Examination of these results leads to the following observations: (1) the deep notch $W/B = 1$ and 2 trajectories are nearly identical for $n = 10$ with a somewhat larger difference for $n = 5$; (2) side grooves in the $W/B = 2$ deep and shallow notch configurations provide small increases of constraint on the midplane at high deformation levels and have insignificant effect early in the loading; (3) deep notch specimens having $W/B = 4$ show a severe constraint loss on the midplane upon initial loading while the relative effect in shallow notch configurations is much less severe; (4) all of the shallow notch J - Q trajectories fall within a relatively narrow band of very low constraint; (5) strain hardening variations from $n = 5 \rightarrow 10$ have a small effect on the 2-D and 3-D J - Q trajectories at higher loads—for a specified J -value, reduced hardening does make Q more negative. Further examination reveals that strain hardening influences the J - Q trajectories most strongly at low-to-moderate loads. The trajectories for $n = 10$ derived using Q at $r = 1$ and $2 \times J/\sigma_0$ remain identical under increasing load to $J_{avg}/b\sigma_0 = 0.01$ while the trajectory for $n = 5$ derived using Q at $r = J/\sigma_0$ matches the $n = 10$ curves to these loading levels; the $n = 5$ trajectory derived using Q at $r = 2J/\sigma_0$ falls below these others. Figures 8 (a) and (b) show this effect as the Q values in these figures are defined at $r = 2J/\sigma_0$.

Figure 9 provides J - Q trajectories for deep notch C(T) specimens. These results lead to the following observations: (1) side grooves have a slight effect of lowering constraint at high load levels on the midplane, see Fig. 9 (a); (2) side-grooves increase constraint significantly at other front locations relative to the plane-sided specimen, compare Figs. 9 (b) and (d); (3) strain hardening affects constraint somewhat for the standard $W/B = 2$ specimen at high loads with a larger effect for the thin specimen $W/B = 4$; (4) SSY conditions exist strictly for deformation levels $b > 100J_{avg}/\sigma_0$ in the standard $W/B = 2$ configuration. The increased elastic T -stress of the C(T) specimen relative to the deep notch SE(B) specimen leads to the 25% increase in deformation before SSY conditions breakdown; $\beta = T\sqrt{\pi a}/K_I = 0.58$ for the C(T) with $a/W = 0.6$ compared to $\beta = 0.15$ for the SE(B) with $a/W = 0.5$ [28].

4.3 Crack Front Stress Triaxiality: Toughness Scaling Model

Figures 10–13 provide descriptions of crack front constraint for plane-sided, deep and shallow notch SE(B) specimens in terms of the toughness scaling model for the practically important cases of $W/B = 1, 2$ and $n = 5, 10$. Figures 14–15 provide similar results for plane-sided ($n = 5, 10$) and side-grooved ($n = 10$) C(T) specimens having $a/W = 0.6$. Results for the side-grooved SE(B) specimens do not provide additional insight and are omitted to conserve space.

Using the previous J - Q trajectories for guidance, we construct the scaling model for a range of $\bar{\sigma}_c$ values at crack front positions of maximum constraint for the SE(B) specimens in Figures 10–13 (a), (b). Maximum constraint occurs on the midplane for all configurations except

$W/B = 1$, $a/W = 0.1$ (maximum constraint at $x_3/(B/2) \approx 0.3-0.65$ with numerical results given here at 0.53). Each figure also includes the result at a $\bar{\sigma}_c$ value obtained from the plane-strain analysis of the specimen. The 3-D J_0 -values are computed from (local) J_{max} -values at the crack front location using the procedures described in Section 2.2 and Eq. (6). However, to connect more directly with experimental work, the abscissa expresses specimen deformation in terms of J_{avg} rather than J_{max} , where J_{avg} represents the conventional J -value reported using a plastic η -factor. A ratio of plastic η -factors, η_{pl-max}/η_{pl} , computed using values shown in Table 1 provides a very good approximation for J_{max}/J_{avg} . For strain hardening $n = 5$, we consider $\bar{\sigma}_c$ values over the range 3.5–4.5 to maintain principal stress contours within a distance of $6-8 \times$ CTOD on the crack plane but outside of the blunting region of $1-2 \times$ CTOD (our FE analyses do not model the LGC of blunting so we exclude contours that would lie inside this region). For the lower strain hardening material, $n = 10$, $\bar{\sigma}_c$ values must be in the range 2.6–3.6 to meet these requirements. For reference, the LGC analyses of SSY predict peak stresses of $4.4\sigma_0$ for $n = 5$ and $3.6\sigma_0$ for $n = 10$ [15,44]. Fractographic studies confirm that cleavage initiation sites rarely occur at distances from the crack front greater than $6-8 \times$ CTODs or at locations deep within the blunting region [19,34].

Figures 10–13 (c), (d) examine more directly the dependence of the scaling model on the range of principal stress ratios, $\bar{\sigma}_c$, applicable for the specified levels of strain hardening; part (c) is constructed from part (a), and part (d) from part (b) in each case where J_{avg}/J_0 is given by the inverse slope of a line from the origin to each point on the curves.

All deep notch SE(B)s show a strong dependence on $\bar{\sigma}_c$ once large-scale yielding conditions prevail but with a smaller dependence for the high hardening ($n = 5$) material. Strain hardening has a much greater (relative) effect on the toughness scaling model than on the J - Q trajectories once SSY breaks down, i.e., for SE(B)s with lower hardening materials, large increments of applied J are needed to produce small changes in J_0 -values. The dependence of the scaling model on $\bar{\sigma}_c$ at very large deformations makes applications to correct for constraint loss in deep notch SE(B)s questionable; although it appears for moderate-to-high hardening materials that useful engineering approximations are possible at deformation levels in the range $J_{avg}/b\sigma_0 \approx 0.01-0.015$. In Fig. 10 (c), for example, at $J_{avg}/b\sigma_0 = 0.01$, J_{avg}/J_0 varies from 1.5 to 1.0 over the range of $\bar{\sigma}_c$. The scaling model clearly maintains sufficient independence of $\bar{\sigma}_c$ early in the loading to support proposals for size/deformation limits ($b > MJ_{avg}/\sigma_0$) to insure SSY conditions at fracture although the gradual loss of constraint introduces some subjectivity into this process. Consider the $n = 10$ and 5 solutions in Figs. 10 (c) and 12 (c) for $W/B = 1$ and allow a mean deviation from strict SSY of $J_{avg}/J_0 = 1.1$ over the range of $\bar{\sigma}_c$ values; M has the values of 85 for $n = 10$ and 35 for $n = 5$; we adopt the notation $M_{1.1}$ to denote these deformation limits. By allowing J_{avg}/J_0 to reach 1.2, $M_{1.2} = 60$ for $n = 10$ and 25 for $n = 5$. Table 3 summarizes similar evaluations of M for all deep notch SE(B) analyses with the plane-strain values included for reference. M values for the 3-D analyses are seen to be substantially more generous (smaller) for fracture testing than the $M \approx 200$ value derived from the earlier plane-strain models of these specimens. The lower M values imply a significantly increased measuring capacity in terms of J_c and CTOD for a given specimen size.

For all of the shallow notch SE(B) configurations, applications of the scaling model to correct for constraint loss appear much more promising with a strong independence on $\bar{\sigma}_c$ to J_{avg}/J_0 ratios approaching 6–7 for $n = 10$ and 4–5 for $n = 5$. The plane-strain solutions do a remarkably good job especially for the $n = 5$ material and less so for the $n = 10$ material. Early applications of the plane-strain version of the scaling model in experimental work focused on

high-hardening materials with $W/B = 1, 2$ but the relevance of plane-strain modeling clouded the conclusions; these 3-D results confirm the applicability of those early plane-strain analyses.

Figures 14 and 15 show results in the same format for the plane-sided and side-grooved C(T) specimens. The C(T)s respond essentially the same as deep notch SE(B)s with very minor effects of the side grooves on the scaling model at the midplane. At low deformation levels for $n = 10$, the plane-strain solution overestimates constraint (J_0 too large) while at larger deformations it underestimates constraint when comparing scaling curves for the same $\bar{\sigma}_c$ (J_0 too small). For $n = 5$, the plane-strain solution underestimates J_0 over the complete loading. However, the plane-strain solution agrees better with the 3-D model for the C(T) specimen than for the deep notch SE(B); see for example Fig. 10 (a). Repeating the same procedure outlined above to define size/deformation limits (M) for the SE(B), we determine the M values summarized in Table 3 for the C(T) specimens. In all cases, the C(T) specimens have smaller M values than for corresponding SE(B) specimens having the same W/B and n which imply the maintenance of SSY conditions to greater levels of deformation.

4.4 Effective Thicknesses

Figures 16 (a) and (b) illustrate the evolution under increased load of the areas enclosed within the principal stress contour $\bar{\sigma}_c = \sigma_1/\sigma_0 = 3$ in the deep and shallow notch SE(B) configurations for $W/B = 1, n = 10$. The front location at which A_{max} occurs has maximum constraint, and we propose B_{eff} given by V/A_{max} , with V from Eq. (9), as the effective specimen thickness subjected to that same (maximum) level of constraint. Consistent with the J - Q trajectories and the scaling model, A_{max} occurs on the midplane for all configurations except the shallow crack SE(B) with $B = W$ as shown in Fig. 16 (b).

Figures 16 (c) and (d) show that B_{eff}/B decreases from near unity under linear elastic conditions to a nearly deformation independent (saturation) value once large-scale yielding conditions develop. Moreover, B_{eff}/B remains reasonably insensitive to a wide-range of $\bar{\sigma}_c$ values examined in the computations. The B_{eff}/B ratio varies significantly with W/B for fixed a/W and material flow characteristics; the ratio decreases with increasing W/B while greater amounts of strain hardening elevate values of B_{eff}/B . The deformation levels at which B_{eff}/B ratios reach the saturation values are identified closely with the loss of SSY conditions for both the deep and shallow notch specimens—compare deformation levels in Figs. 10 (a), (b) at which J_{avg} first exceeds J_0 with attainment of saturation values in Figs. (c) and (d). Table 4 provides these saturation values of B_{eff}/B , obtained by rough averaging over the $\bar{\sigma}_c$ values, for all specimens analyzed and the approximate deformation levels at which the saturation values are reached.

Effective thicknesses for plane-sided and side-grooved C(T) specimens with $a/W = 0.6$ and $n = 10$ are given in Fig. 17 (a). Even though the side-grooving process removes 20% of the crack front material, the B_{eff}/B ratios remain very similar (0.53 for SGs vs. 0.47 for plane-sided). The plane-sided and side-grooved SE(B) specimens with deep notches, as shown in Fig. 17 (b), follow the same trend (0.5 for side-grooved vs. 0.45 for plane-sided). These results, when combined with the previously shown identical scaling model response, suggests there should be a minimal effect of side grooves on measured J_c values. Experimental programs have reported essentially no difference in plane-sided and side-grooved J_c -values over the DBT region in the absence of prior ductile tearing (see [18,59] for example data sets).

Finally, Fig. 18 illustrates the differences introduced in the thickness correction model of Eq. (8) through the use of actual thicknesses rather than effective thicknesses. In each configuration, the simple ratio of actual thicknesses appears to undercorrect measured J_c -values, i.e., $\sqrt{B_{eff(1)}/B_{eff(2)}}$ is greater than $\sqrt{B_{(1)}/B_{(2)}}$ by 40% in the extreme case but only by 10% for deep notch SE(B)s for an $n = 5$ material. The difference in using actual vs. effective thickness ratios increases with the amount of strain hardening and decreases with a/W ratio. These comparisons apply to fixed planform specimen dimensions and varying thicknesses (W/B). Of course, when specimens with fixed a/W and W/B ratios are scaled proportionally, the effective thicknesses play no role as $\sqrt{B_{eff(1)}/B_{eff(2)}} = \sqrt{B_{(1)}/B_{(2)}}$. Validation of the predictions by the model shown in Fig. 18 await applications to experimental data sets generated in the DBT region for materials and specimens with these characteristics.

5. Summary and Conclusions

An extensive set of nonlinear, 3-D finite element analyses of SE(B) and C(T) specimens performed in this investigation reveal a complex interaction between the geometric ratios, a/W and W/B , and material hardening properties on the crack front J and stress distributions. The analyses provide a new set of plastic η -factors for use in experimental work to relate work done on the remaining ligament at fracture to thickness average J -values and to maximum (local) J -values over the crack front. A corresponding set of 3-D based m -factors is provided for use in the conversion between crack front maximum CTOD values and (local) J -values ($J = m\sigma_{flow}\delta$).

The detailed element meshes enabled evaluation of crack front constraint in terms of J - Q trajectories and the toughness scaling model. An extension of the earlier plane-strain version of the scaling model is proposed which combines an "in-plane" correction at the crack front location of maximum stress triaxiality coupled with a thickness correction derived from extreme value statistics applicable for ferritic materials which fail by cleavage in the ductile-to-brittle transition region.

For deep notch SE(B) and C(T) specimens, the 3-D analyses demonstrate that midplane levels of stress triaxiality are maintained at SSY conditions to higher deformation levels than predicted by earlier plane-strain analyses. Equipping the $W/B = 2$ SE(B) and C(T) specimens with 20% side grooves does not significantly alter the midplane stresses but does restore nearly uniform stresses at each crack front location such that B_{eff}/B for the side-grooved specimens slightly exceeds the plane-sided B_{eff}/B values. Interpretation of the computational results in these forms leads us to three specific recommendations: (1) the size/deformation limit for cleavage fracture in the DBT region in deep notch SE(B) and C(T) specimens having strong-to-moderate hardening ($n = 5-10$) should be $b > MJ_c/\sigma_0$ with $M = 25-50$ rather than $M = 200$ as previously recommended from the plane-strain analyses; (2) use of the plane-strain form of the toughness scaling model overcorrects measured J_c -values for constraint loss—the 3-D based correction curves given here should be used; and (3) effective (B_{eff}), rather than actual specimen thicknesses (B), are suggested for use in the statistical correction to accommodate the effects of varying W/B , a/W ratios and material strain hardening.

6. References

1. Al-Ani, A.M., and Hancock, J.W., "J-Dominance of Short Cracks in Tension and Bending," *Journal of Mechanics and Physics of Solids*, Vol. 39, pp. 23-43, 1991.[†]

2. Anderson, T.L., and Dodds, R.H., "Specimen Size Requirements for Fracture Toughness Testing in the Ductile-Brittle Transition Region," *Journal of Testing and Evaluation*, Vol. 19, pp. 123-134, 1991.[†]
3. Anderson, T. L. *Fracture Mechanics: Fundamentals and Applications*. CRC Press, Boston, 1994.[†]
4. Batdorf, S. B. and Crose, J. G., "A Statistical Theory for the Fracture of Brittle Structures Subjected to Nonuniform Polyaxial Stresses," *Journal of Applied Mechanics*, Vol. 41, pp. 459-464, 1974.[†]
5. Beremin, F.M., "A Local Criterion for Cleavage Fracture of a Nuclear Pressure Vessel Steel," *Metalurgical Transactions*, Vol. 14A, pp. 2277-2287, 1983.[†]
6. Betegon, C., and Hancock, J.W., "Two-Parameter Characterization of Elastic-Plastic Crack Tip Fields," *Journal of Applied Mechanics*, Vol. 58, pp. 104-113, 1991.[†]
7. Bilby, B.A., Cardew, G.E., Goldthorpe, M.R. and Howard, I.C., "Size Effects in Fracture," *Institution of Mechanical Engineers*, London, England, pp. 36-46, 1986.[†]
8. Brocks, W. and Olschewski, J., "On J -Dominance of Crack-Tip Fields in Largely Yielded 3D Structures," *International Journal of Solids and Structures*, Vol. 22, pp. 693-708, 1986.[†]
9. Bruckner-Foit, A., Ehl, W., Munz, D. and Trolldenier, B., "The Size Effect of Microstructural Implications of the Weakest Link Model," *Fatigue and Fracture of Engineering Materials and Structures*, Vol. 13, pp. 185-200, 1990.[†]
10. Chao, Y.J. and Sutton, M.A., "On the Fracture of Solids Characterized by One or Two Parameters," *Journal of Mechanics and Physics of Solids*, Vol. 42, pp. 629-647, 1994.[†]
11. Curry, D.A., and Knott, J.K., "Effect of Microstructure on Cleavage Fracture Toughness in Mild Steel," *Metal Science*, Vol. 13, pp. 341-345, 1979.[†]
12. DeCastro, P.M.S.T., Spurrire, J., and Hancock, P., "An Experimental Study of the Crack Length / Specimen Width (a/W) Ratio Dependence of the Crack Opening Displacement (COD) Test Using Small-Scale Specimens," *Fracture Mechanics, ASTM STP 677*, C.W. Smith, Ed., American Society for Testing and Materials, Philadelphia, Pennsylvania, pp. 486-497, 1979.[†]
13. deLorenzi, H. and Shih, C.F., "3-D Elastic Plastic Investigation of Fracture Parameters in a Side-Grooved Compact Specimen," *International Journal of Fracture*, Vol. 13, pp. 195-220, 1983.[†]
14. Dodds, R.H., Anderson, T.L., and Kirk, M.T., "A Framework to Correlate a/W Ratio Effects on Elastic-Plastic Fracture Toughness (J_c)," *International Journal of Fracture*, Vol. 48, pp. 1-22, 1991.[†]
15. Dodds, R. H., Shih, C. F., and Anderson, T. L., "Continuum and Micro-Mechanics Treatment of Constraint in Fracture," *International Journal of Fracture*, Vol. 64, pp. 101-133, 1993.[†]
16. Du, Z.-Z., and Hancock, J.W., "The Effect of Non-Singular Stresses on Crack-Tip Constraint," *Journal of Mechanics and Physics of Solids*, Vol. 39, pp. 555-567, 1991.[†]
17. Evans, A. G., 1978, "A General Approach for the Statistical Analysis of Multiaxial Fracture," *Journal of American Ceramic Society*, Vol. 61, pp. 302-308, 1978.[†]
18. Faucher, B. and Tyson, W.R., "Size Limits for Brittle Fracture Toughness of Bend Specimens," in *Constraint Effects in Fracture, ASTM STP 1171*, Hackett, et al. Eds., American Society for Testing and Materials, Philadelphia, pp. 306-317, 1993.[†]
19. Herrens, J., and Read, D.T., "Fracture Behavior of a Pressure Vessel Steel in the Ductile-to-Brittle Transition Region," NISTIR 88-3099, National Institute for Standards and Technology, Boulder, Colorado, December, 1988.*
20. Hughes, T. J. "Generalization of Selective Integration Procedures to Anisotropic and Nonlinear Media," *International Journal for Numerical Methods in Engineering*, Vol. 15, pp. 1413-1418, 1980.
21. Hughes, T. J., Levit, I., and Winget, J. M., "An Element-By-Element Solution Algorithm for Problems of Structural and Solid Mechanics," *Computer Methods in Applied Mechanics and Engineering*, Vol. 36, pp. 241-254, 1983.[†]
22. Hughes T.J.R., Ferencz R.M., and Hallquist J.O., "Large-Scale Vectorized Implicit Calculations in Solid, Mechanics on a Cray X-MP/48 Utilizing EBE Preconditioned Conjugate Gradients," *Computer Methods in Applied Mechanics and Engineering*, Vol. 61, pp. 215-248, 1987.[†]
23. Hutchinson, J.W., "Fundamentals of the Phenomenological Theory of Nonlinear Fracture Mechanics," *Journal of Applied Mechanics*, Vol. 50, pp. 1042-1051, 1983.[†]
24. Ingham, T., Knee, N., Milne, I., and Morland, E., "Fracture Toughness in the Transition Regime for A533B Steel: Prediction of Large Specimen Results from Small Specimen Tests," *Fracture Mechanics: Perspectives and Directions: Twentieth Symposium ASTM STP 1020*, R.P. Wei and R. Gangloff Eds., American Society for Testing and Materials, Philadelphia, pp. 369-389, 1989.[†]

25. Kirk, M.T. and Dodds, R.H., "J and CTOD Estimation Equations for Shallow Cracks in Single Edge Notch Bend Specimens," *Journal of Testing and Evaluation*, Vol. 24, No. 4, pp. 228-238, 1993.[†]
26. Koers, R., Braam, H., and Bakker, A., "Investigation into the Effects of Thickness on Three- and Four-Point SE(B) Specimens Using 2-D and 3-D Elastic-Plastic Stress Analyses," *Proceedings, 7th International Conference on Fracture (ICF7)*, Houston, Texas, pp. 379-389, 1989.[†]
27. Koppenhoefer, K., Gullerud, A., Ruggieri, C., Dodds, R. and Healy, B., "WARP3D: Dynamic Non-linear Analysis of Solids Using a Preconditioned Conjugate Gradient Software Architecture," *Structural Research Series (SRS) 596*, UILU-ENG-94-2017, University of Illinois at Urbana-Champaign, 1994.[†]
28. Leever, P. S., and Radon, J.C., "Inherent Stress Biaxiality in Various Fracture Specimen geometries," *International Journal of Fracture*, Vol. 19, pp. 311-325, 1982.[†]
29. Li, F.Z., Shih, C.F., and Needleman, A., "A Comparison of Methods for Calculating Energy Release Rates," *Engineering Fracture Mechanics*, Vol. 21, pp. 405-421, 1985.[†]
30. Li, Y.C., and Wang, T.C., "Higher-Order Asymptotic Field of Tensile Plane-Strain Nonlinear Crack Problem," *Scientia Sinica (Series A)*, Vol. 29, pp. 941-955, 1986.[†]
31. Lin, T., Evans, A. G. and Ritchie, R. O., 1986, "A Statistical Model of Brittle Fracture by Transgranular Cleavage," *Journal of Mechanics and Physics of Solids*, Vol. 21, pp. 263-277, 1986.[†]
32. Machida, K., Kikuchi, M., and Miyamoto, H., "J Integral Evaluation of Side-Grooved CCT Specimens by Three-Dimensional Analyses," *Analytical, Numerical and Experimental Aspects of Three-Dimensional Fracture Processes*, AMD-Vol. 91, ASME, pp. 309-319, 1988.[†]
33. McMeeking, R.M., and Parks, D.M., "On Criteria for J-Dominance of Crack-Tip Fields in Large-Scale Yielding," *Elastic-Plastic Fracture*, ASTM STP 668, J.D. Landes, J.A. Begley, and G.A. Clark, Eds., American Society for Testing and Materials, Philadelphia, Pennsylvania, pp.175-194, 1979.[†]
34. Miglin, M.T., Wade, C.S., and Van Der Sluys, W.A., "Analysis of Fracture Toughness Data for Modified SA508 C12 in the Ductile-to-Brittle Transition Region," *Fracture Mechanics: Twenty-First Symposium*, ASTM STP 1074, J.P. Gudas, J.A. Joyce, and E.M. Hackett, Eds., American Society for Testing and Materials, Philadelphia, Pennsylvania, pp. 238-263, 1990.[†]
35. Minami, F., Brückner-Foit, A., Munz, D. and Trollidenier, B., "Estimation Procedure for the Weibull Parameters Used in the Local Approach," *International Journal of Fracture*, Vol. 54, pp. 197-210, 1992.
36. Moran, B., and Shih, C.F., "Crack Tip and Associated Domain Integrals from Momentum and Energy Balance," *Engineering Fracture Mechanics*, Vol. 27, pp. 615-642, 1987.[†]
37. Moran, B., and Shih, C.F., "A General Treatment of Crack Tip Contour Integrals," *International Journal of Fracture*, Vol. 35, pp. 295-310, 1987.[†]
38. Morland, E., "Fracture Toughness in the Transition Regime for A533B-1 Steel: The Effect of Specimen Sidegrooving," *Fracture Mechanics: Twenty-First Symposium*, ASTM STP 1074, J.P. Gudas, et al. Eds., American Society for Testing and Materials, Philadelphia, pp. 215-237, 1990.[†]
39. Mudry, F., "A Local Approach to Cleavage Fracture," *Nuclear Engineering and Design*, Vol. 105, pp. 65-76, 1987.
40. Nagtegaal, J. C. Parks, D. M., and Rice, J. R., "On Numerically Accurate Finite Element Solutions in the Fully Plastic Range," *Computer Methods in Applied Mechanics and Engineering*, Vol. 4, pp. 153-178, 1974.[†]
41. Nakamura, T., and Parks, D. M., "Determination of the Elastic T-Stress Along 3-D Crack Fronts Using an Interaction Integral," *International Journal of Solids and Structures*, Vol. 29, pp. 1597-1611, 1992.[†]
42. Narasimhan, R., Rosakis, A.J., and Zehnder, A.T., "Three-Dimensional Fields for a Through Crack in an Elastic-Plastic Solid: Numerical Analysis and Comparison with Interferometric Measurements," *Analytical, Numerical and Experimental Aspects of Three-Dimensional Fracture Processes*, AMD-Vol. 91, ASME, pp. 239-254, 1988.[†]
43. Nevalainen, M. and Wallin, K., "The Effect of Crack Depth and Absolute Thickness on Fracture Toughness of 3PB Specimens". *ECF 10 - Structural Integrity: Experiments, Models and Applications*, Vol. 2. K-H. Schwalbe and C. Berger, Eds., European Structural Integrity Society, Berlin, pp. 997-1006, 1994.[†]

44. O'Dowd, N.P., and Shih, C.F., "Family of Crack-Tip Fields Characterized by a Triaxiality Parameter: Part I – Structure of Fields," *Journal of the Mechanics and Physics of Solids*, Vol. 39., No. 8, pp. 989–1015, 1991.[†]
45. O'Dowd, N.P., and Shih, C.F., "Family of Crack-Tip Fields Characterized by a Triaxiality Parameter: Part II – Fracture Applications," *Journal of the Mechanics and Physics of Solids*, Vol. 40, pp. 939–963, 1992.[†]
46. Parks, D.M., "Advances in Characterization of Elastic-Plastic Crack-Tip Fields," in *Topics in Fracture and Fatigue*, A. S. Argon, Ed., Springer Verlag, pp. 59–98, 1992.[†]
47. Rice, J.R., "A Path Independent Integral and the Approximate Analysis of Strain Concentration by Notches and Cracks," *Journal of Applied Mechanics*, Vol. 35, pp. 379–386, 1968.[†]
48. Ritchie, R.O., Knott, J.F., and Rice, J.R., "On the Relationship Between Critical Tensile Stress and Fracture Toughness in Mild Steel," *Journal of Mechanics and Physics of Solids*, Vol. 21, pp. 395–410, 1973.[†]
49. Sharma, S.M. and Aravas, N. *Journal of Mechanics and Physics of Solids*, Vol. 39, pp. 1043–1072, 1991.[†]
50. Shih, C.F. and German, M.D., "Requirements for a One Parameter Characterization of Crack Tip Fields by the HRR Singularity," *International Journal of Fracture*, Vol. 17, No. 1, pp. 27–43, 1981.[†]
51. Shih, C.F., Moran, B., and Nakamura, T. "Energy Release Rate Along a Three-Dimensional Crack Front in a Thermally Stressed Body," *International Journal of Fracture*, Vol. 30, pp. 79–102, 1986.[†]
52. Sorem, W.A., Dodds, R.H., and Rolfe, S.T., "Effects of Crack Depth on Elastic Plastic Fracture Toughness," *International Journal of Fracture*, Vol. 47, pp. 105–126, 1991.[†]
53. Theiss, T.J., and Bryson, J.W., "Influence of Crack Depth on the Fracture Toughness of Reactor Pressure Vessel Steel," in *Constraint Effects in Fracture, ASTM STP 1171*, E.M. Hackett, et al. Eds., American Society for Testing and Materials, Philadelphia, pp. 104–119, 1993.[†]
54. Wallin, K., Saario, T., and Torronen, K., "Statistical Model for Carbide Induced Brittle Fracture in Steel," *Metal Science*, Vol. 18, pp. 13–16, 1984.[†]
55. Wallin, K. "The Scatter in K_{Ic} Results," *Engineering Fracture Mechanics*, Vol. 19, pp. 1085–1093, 1984.[†]
56. Wallin, K. "The Size Effect in K_{Ic} Results," *Engineering Fracture Mechanics*, Vol. 22, pp. 149–163, 1985.[†]
57. Wallin, K. "The Effect of Ductile Tearing on Cleavage Fracture Probability in Fracture Toughness Testing," *Engineering Fracture Mechanics*, Vol. 32, pp. 523–531, 1989.[†]
58. Wallin, K., "Statistical Modelling of Fracture in the Ductile-to-Brittle Transition Region," in *Defect Assessment in Components—Fundamentals and Applications, ESIS/EGF9*, J.G. Blauel and K.-H. Schwalbe, Eds., Mechanical Engineering Publications, London, pp. 415–445, 1991.[†]
59. Wallin, K., "Statistical Aspects of Constraint with Emphasis on Testing and Analysis of Laboratory Specimens in the Transition Region," in *Constraint Effects in Fracture, ASTM STP 1171*, Hackett, et al. Eds., American Society for Testing and Materials, Philadelphia, pp. 264–288, 1993.[†]
60. Wang, Y.Y., "A Two-Parameter Characterization of Elastic-Plastic Crack-Tip and Applications to Cleavage Fracture," Ph.D. Thesis, Department of Mechanical Engineering, MIT, 1991.[†]
61. Wang, Y.Y., and Parks, D. M., "Evaluation of the Elastic T -Stress in Surface Cracked Plates Using the Line-Spring Method," *International Journal of Fracture*, Vol. 56, pp. 25–40, 1992.[†]
62. Wang, Y.Y., "On the Two-Parameter Characterization of Elastic-Plastic Crack-Front Fields in Surface-Cracked Plates," in *Constraint Effects in Fracture, ASTM STP 1171*, Hackett, et al. Eds., American Society for Testing and Materials, Philadelphia, pp. 120–138, 1993.[†]
63. Williams, M.L., *Journal of Applied Mechanics*, Vol. 24, pp. 109–114, 1957.[†]
64. Yang, S., Chao, Y.J. and Sutton, M.A., "Higher Order Terms in Two-Dimensional Analysis of Crack Tip Fields in Elastic-Plastic Bodies," *Engineering Fracture Mechanics*, Vol. 45, pp. 1–20, 1993.[†]

* Available for purchase from National Technical Information Service, Springfield, VA 22161.

† Available from public technical libraries.

‡ Copies are available from U.S. Government Printing Office, Washington, D.C. 20402. ATTN:
Regulatory Guide Account.

Table 1. Plastic η factors for SE(B) and C(T) specimens

		SE(B), $a/W=0.1$									
		W/B=4			W/B=2				W/B=1		
		n=5	n=10	n=20	n=5	n=10	n=10 SG	n=20	n=5	n=10	n=20
LLD:	η_{max}	1.46	1.75	1.91	1.19	1.40	1.45	1.56	0.968	1.09	1.19
	η_{avg}	1.21	1.39	1.47	1.07	1.20	1.40	1.28	0.887	0.992	1.07
CMOD:	η_{max}	4.31	4.34	4.46	4.08	4.14	4.30	4.27	3.87	3.76	3.80
	η_{avg}	3.59	3.45	3.43	3.66	3.53	4.17	3.51	3.55	3.41	3.43
	$\eta_{P-Strain}$	3.53	3.45	3.50							

		SE(B), $a/W=0.5$									
		W/B=4			W/B=2				W/B=1		
		n=5	n=10	n=20	n=5	n=10	n=10 SG	n=20	n=5	n=10	n=20
LLD:	η_{max}	2.54	2.69	2.78	2.44	2.51	2.61	2.53	2.24	2.18	2.13
	η_{avg}	1.93	1.90	1.85	1.87	1.84	2.18	1.82	1.89	1.86	1.85
CMOD:	η_{max}	3.50	3.69	3.82	3.45	3.53	3.70	3.57	3.20	3.13	3.07
	η_{avg}	2.65	2.60	2.53	2.64	2.59	3.10	2.57	2.70	2.67	2.66
	$\eta_{P-Strain}$	2.75	2.70	2.69							

		C(T), $a/W=0.6$									
		W/B=4			W/B=2				W/B=1		
		n=5	n=10	n=20	n=5	n=10	n=10 SG	n=20	n=5	n=10	n=20
LLD:	η_{max}	2.91	3.07	3.19	2.78	2.90	3.01	2.87	2.63	2.59	2.57
	η_{avg}	2.21	2.16	2.12	2.17	2.17	2.60	2.15	2.27	2.28	2.28

$$J_{pl-max} = \eta_{max} \frac{U_{pl}}{Bb}; \quad J_{pl-avg} = \eta_{avg} \frac{U_{pl}}{Bb}$$

Full thickness (B) used in η calculations for SG models

U_{pl} from load-line displacement (LLD) or CMOD

Table 2. m -values for CTOD- J relationship: $J_{local} = m\sigma_{flow}\delta_{local}$; $\sigma_{flow} = 1/2(\sigma_y + \sigma_u)$

		SE(B), $a/W=0.1$					
		W/B=4		W/B=2		W/B=1	
@ $x_3/(B/2)$		$n=5$	$n=10$	$n=5$	$n=10$	$n=5$	$n=10$
0.0		2.01	1.78	1.98	1.74	1.89	1.60
0.53		---	---	---	---	1.93	1.64
P. Strain		1.81	1.53				1.50
		SE(B), $a/W=0.5$					
		W/B=4		W/B=2		W/B=1	
@ $x_3/(B/2)$		$n=5$	$n=10$	$n=5$	$n=10$	$n=5$	$n=10$
0.0		2.24	2.08	2.31	2.09	2.25	2.04
P. Strain		2.05	1.80				1.95
		C(T), $a/W=0.6$					
		W/B=4		W/B=2		W/B=1	
@ $x_3/(B/2)$		$n=5$	$n=10$	$n=5$	$n=10$	$n=5$	$n=10$
0.0		2.26	2.09	2.25	2.08	2.25	2.11
							1.91

Table 3. M factors for size/deformation limit in $b \geq M J_{avg} / \sigma_0$

	SE(B), $a/W=0.5$								
	$n=5$			$n=10$			$n=20$		
	$M_{1,0}$	$M_{1,1}$	$M_{1,2}$	$M_{1,0}$	$M_{1,1}$	$M_{1,2}$	$M_{1,0}$	$M_{1,1}$	$M_{1,2}$
$W/B = 1$	70	35	25	125	85	60	400	145	115
$W/B = 2$	50	30	25	120	75	55	*	175	115
$W/B = 2$ SG	—	—	—	*	110	65	—	—	—
P. Strain	175	105	75	215	155	130	340	210	180

	C(T), $a/W=0.6$								
	$n=5$			$n=10$			$n=20$		
	$M_{1,0}$	$M_{1,1}$	$M_{1,2}$	$M_{1,0}$	$M_{1,1}$	$M_{1,2}$	$M_{1,0}$	$M_{1,1}$	$M_{1,2}$
$W/B = 2$	35	25	20	90	60	45	160	115	90
$W/B = 2$ SG	—	—	—	115	80	55	—	—	—
P. Strain	50	35	25	70	60	50	75	65	55

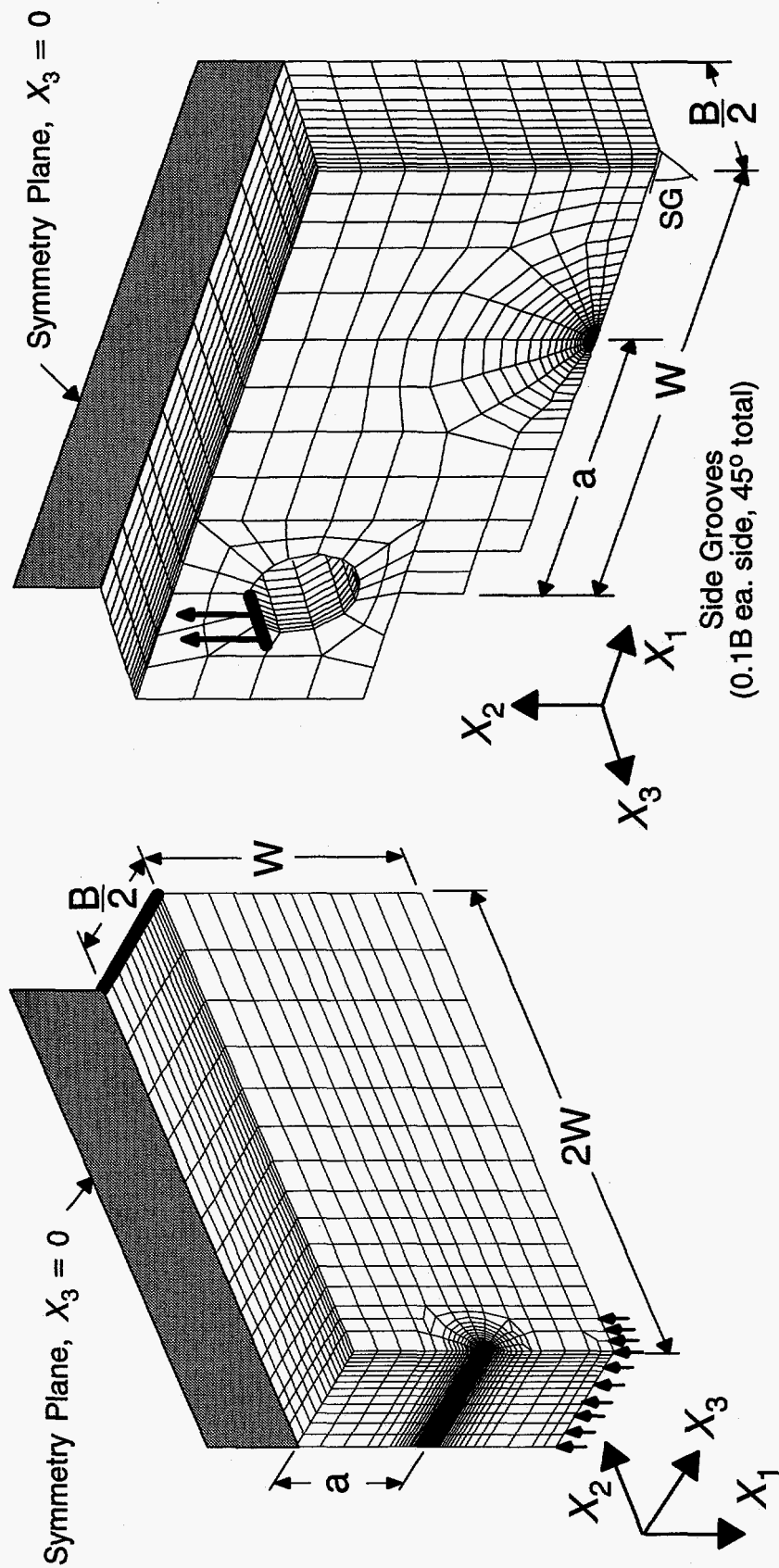
Notes: $M_{1,2}$ denotes, for example, the size/deformation limit at which J_{FB}/J_0 is allowed to reach 1.2

— denotes no finite element analysis available from this study

* indicates no value possible from analysis

Table 4. B_{eff} ratios at saturation and deformation levels

SE(B), $a/W=0.1$										
	W/B=4			W/B=2				W/B=1		
	n=5	n=10	n=20	n=5	n=10	n=10 SG	n=20	n=5	n=10	n=20
B_{eff}/B	0.58	0.46	0.36	0.65	0.52	0.75	0.37	0.79	0.68	0.52
$J_{avg}/a\sigma_0$	0.06	0.06	0.07	0.10	0.12	0.36	0.14	0.07	0.10	0.09
SE(B), $a/W=0.5$										
	W/B=4			W/B=2				W/B=1		
	n=5	n=10	n=20	n=5	n=10	n=10 SG	n=20	n=5	n=10	n=20
B_{eff}/B	0.53	0.43	0.35	0.54	0.45	0.50	0.39	0.66	0.63	0.60
$J_{avg}/b\sigma_0$	0.008	0.011	0.010	0.014	0.015	0.025	0.015	0.016	0.018	0.012
C(T), $a/W=0.6$										
	W/B=4			W/B=2				W/B=1		
	n=5	n=10	n=20	n=5	n=10	n=10 SG	n=20	n=5	n=10	n=20
B_{eff}/B	0.52	0.42	0.35	0.56	0.47	0.53	0.42	0.72	0.70	0.69
$J_{avg}/b\sigma_0$	0.011	0.012	0.015	0.017	0.018	0.030	0.020	0.008	0.008	0.008



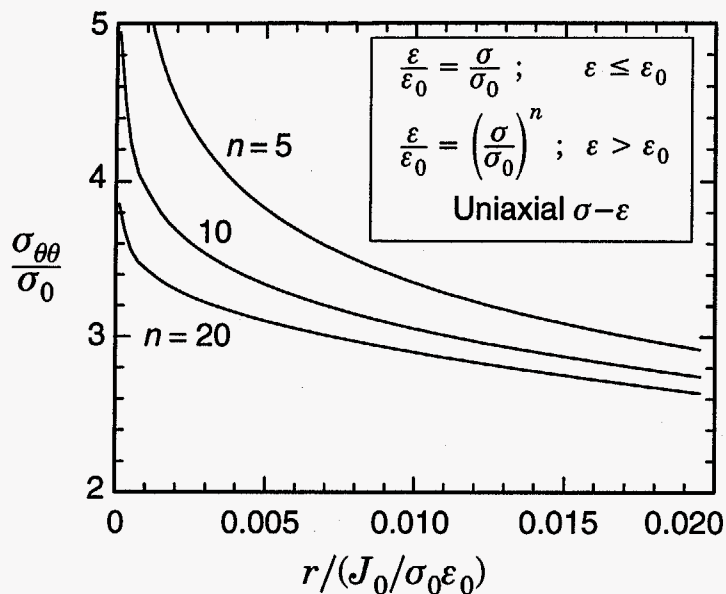
9240 Nodes, 7658 Elements (8-node, \bar{B})
14 Layers for $B/2$

(a)

8085 Nodes, 6566 Elements (8-node, \bar{B})
14 Layers for $B/2$

(b)

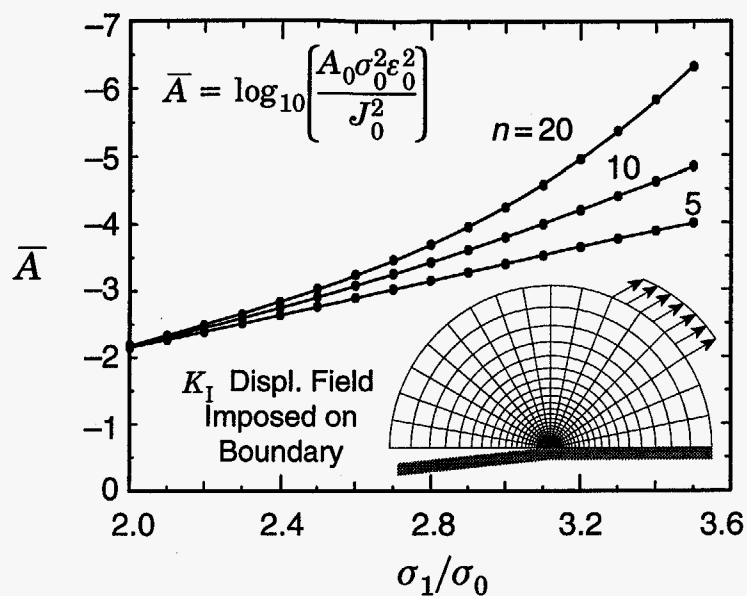
Fig. 1. Typical finite element models for investigation of constraint effects in: (a) SE(B) specimens and (b) C(T) specimens.



<u>Hoop Stress:</u> $\frac{\sigma_{\theta\theta}}{\sigma_0}$			
n	α	β	γ
5	1.5144	-0.17669	-2.0260
10	2.0600	-0.095105	-4.4849
20	2.4904	-0.047627	-6.6943

Fitting Function: $\frac{\sigma_{\theta\theta}}{\sigma_0} = \alpha \hat{r}^\beta \exp(\gamma \hat{r})$

(a)



<u>Contour Areas:</u> \bar{A}					
n	H_0	H_1	H_2	H_3	H_4
5	0.3128	-1.7639	0.4452	-0.1262	0.01211
10	-0.4607	-0.7017	0.1119	-0.1196	0.01227
20	2.7583	-3.5533	0.2896	0.3015	-0.08754

Fitting Function: $\bar{A} = H_0 + H_1 \hat{\sigma} + H_2 \hat{\sigma}^2 + H_3 \hat{\sigma}^3 + H_4 \hat{\sigma}^4$
 ($\hat{\sigma} = \sigma_1 / \sigma_0$)

(b)

Fig. 2. Opening mode stresses on crack plane and principal stress contour areas for SSY ($T=0$, plane-strain).

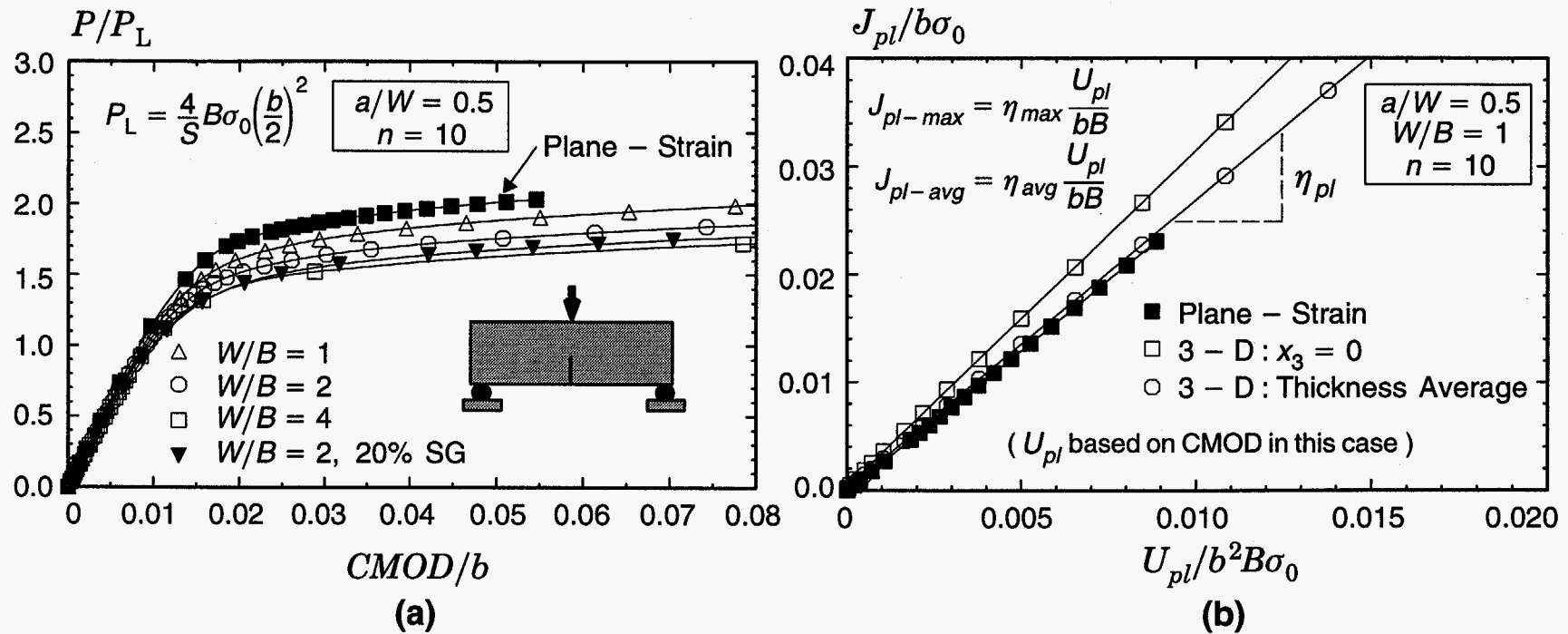


Fig. 3. (a) Normalized load-displacement responses for deep notch SE(B) specimens. (b) Normalized plastic work on remaining ligament used to compute plastic "eta" factors for J estimation. $E/\sigma_0 = 500$, $n = 10$ all analyses.

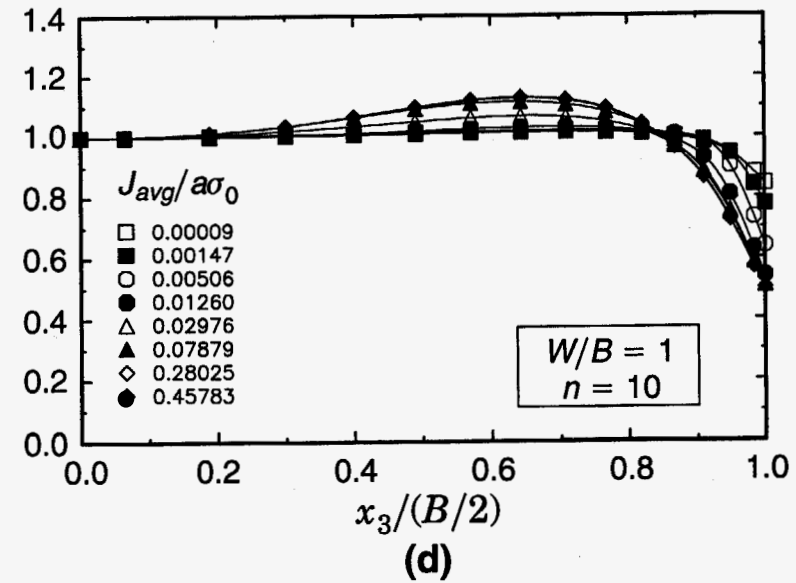
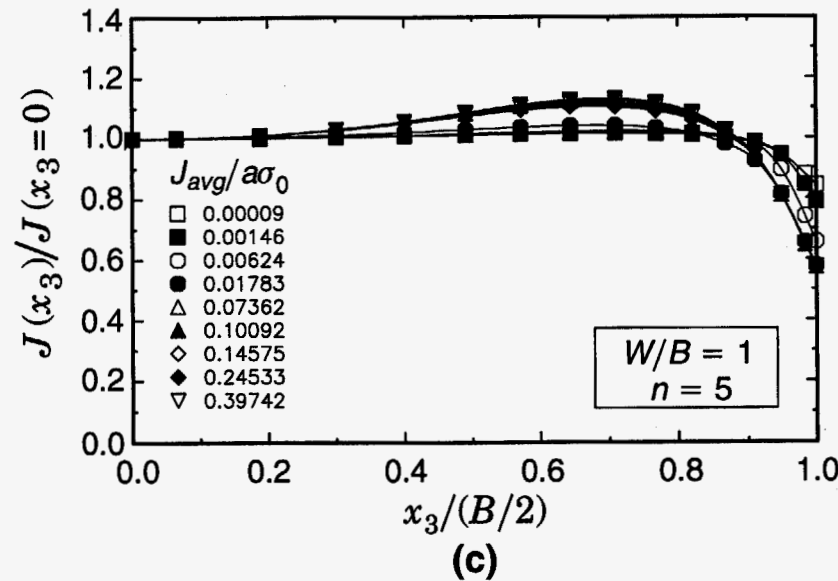
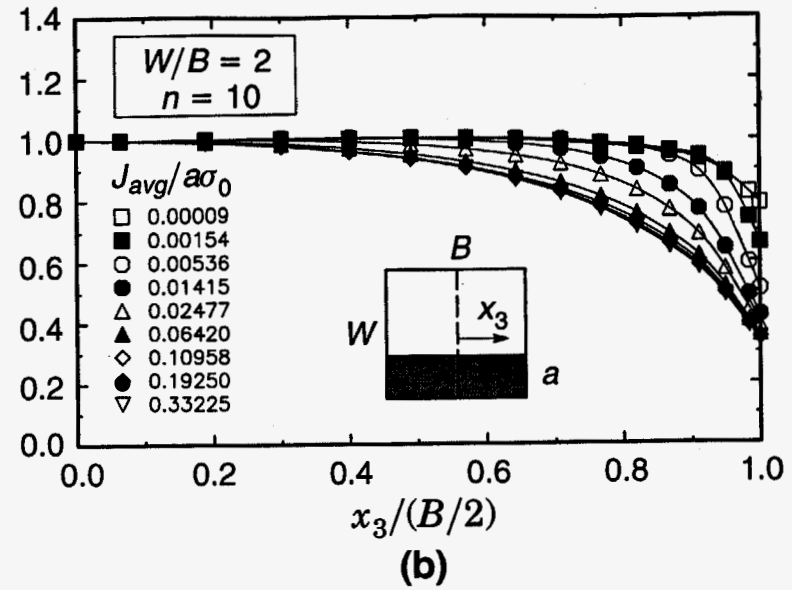
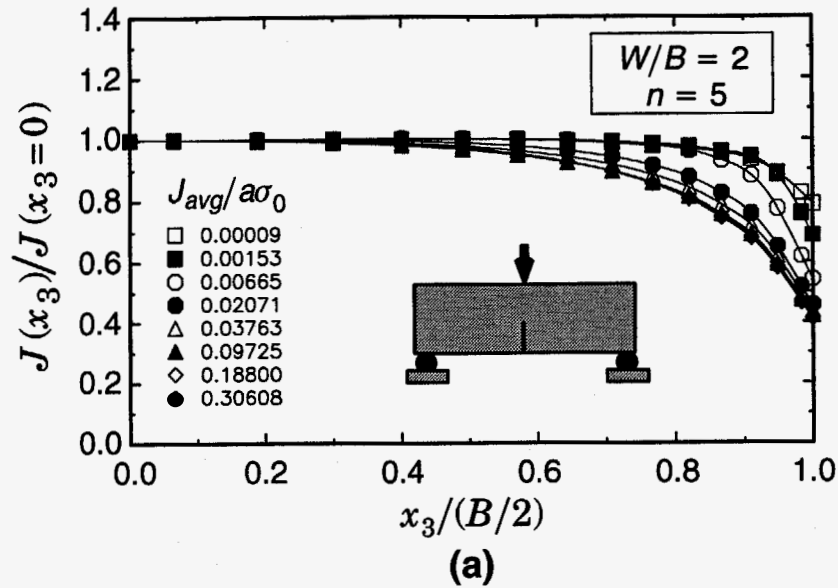


Fig. 4. Distributions of J over crack front for shallow notch SE(B), $a/W=0.1$. (a) $W/B=2, n=5$; (b) $W/B=2, n=10$; (c) $W/B=1, n=5$; (d) $W/B=1, n=10$. $E/\sigma_0=500, \nu=0.3$ all analyses.

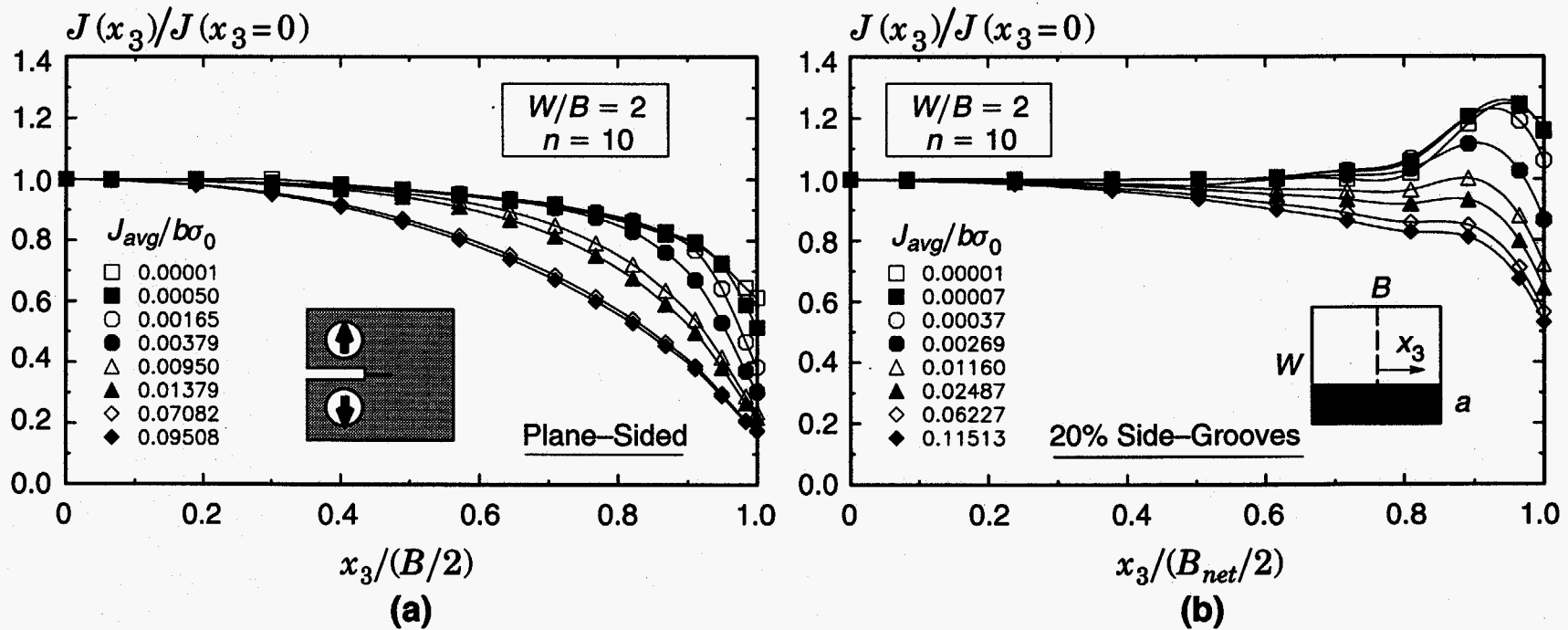


Fig. 5. Distributions of J over crack front for C(T) specimens, $a/W = 0.6$, $W/B = 2$, $n = 10$; (a) plane-sided specimen, (b) specimen with 20% side grooves. $E/\sigma_0 = 500$, $\nu = 0.3$ all analyses.

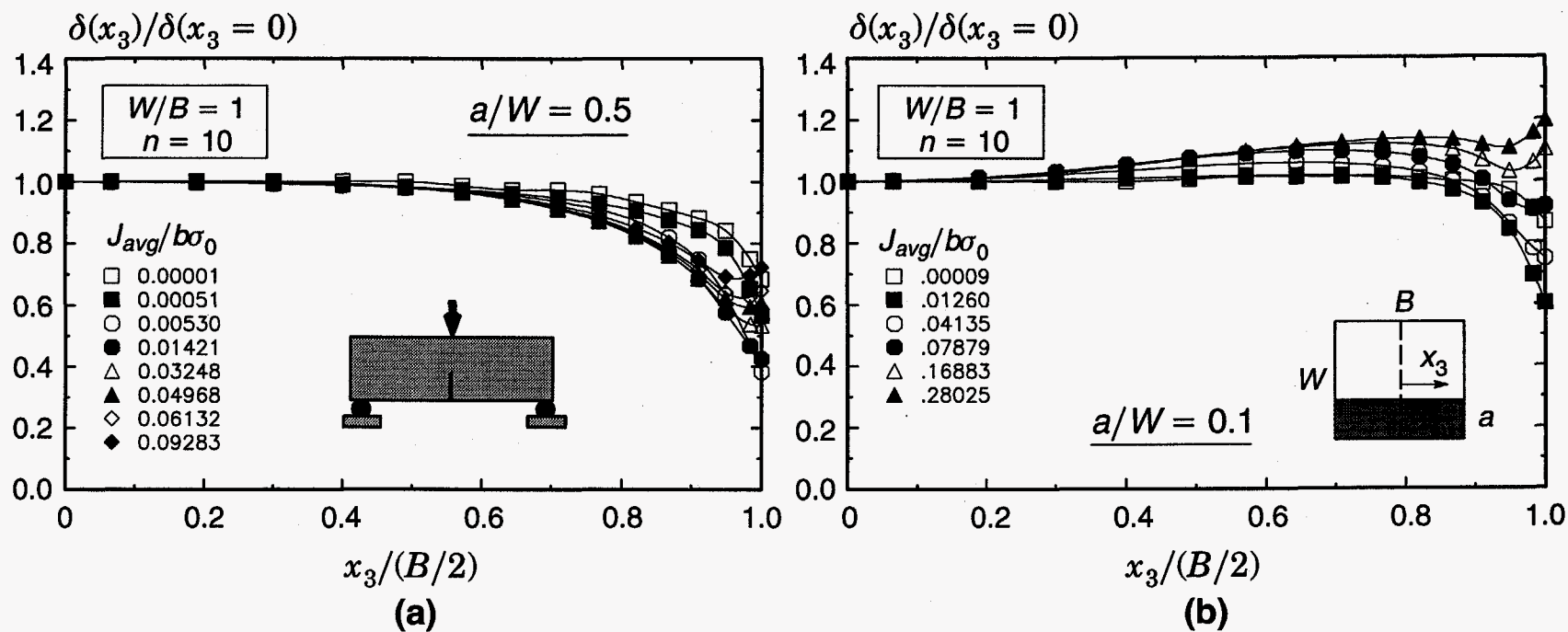


Fig. 6. Distributions of CTOD over crack front for plane-sided SE(B) specimens, $W/B=1$, $n=10$. (a) $a/W=0.5$, (b) $a/W=0.1$. $E/\sigma_0=500$, $\nu=0.3$ all analyses.

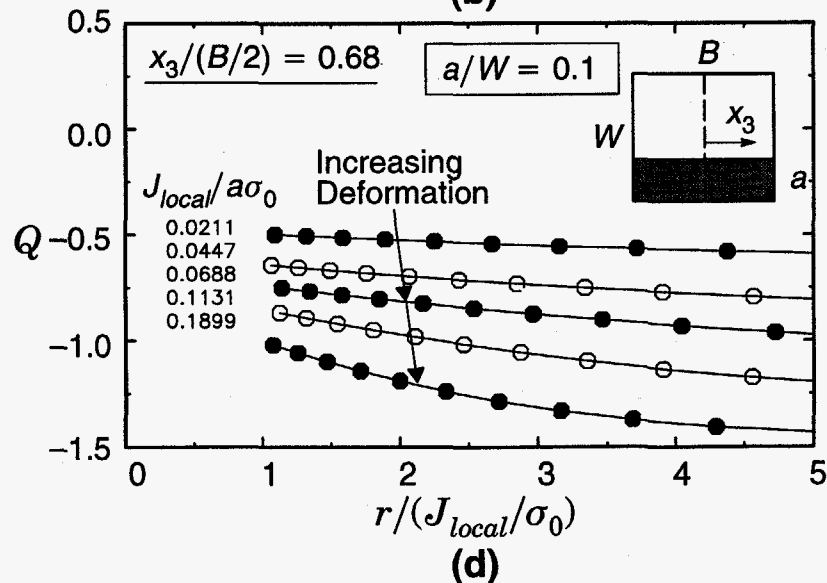
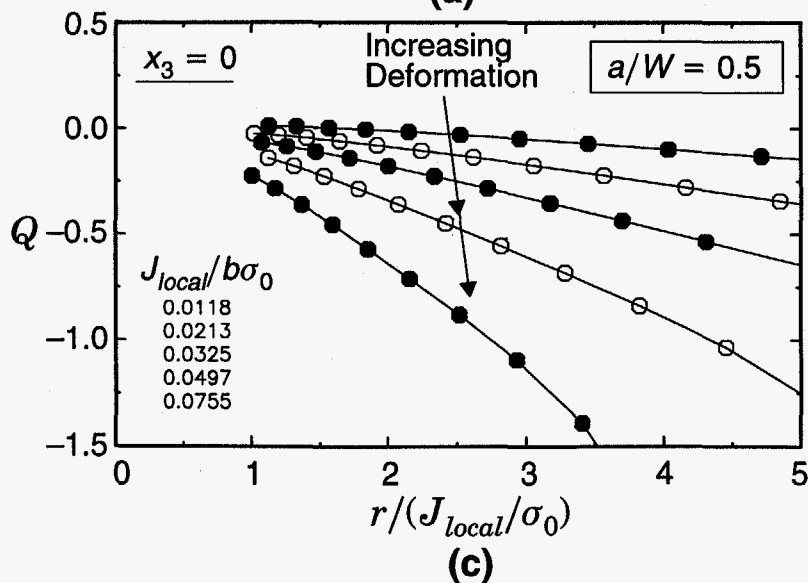
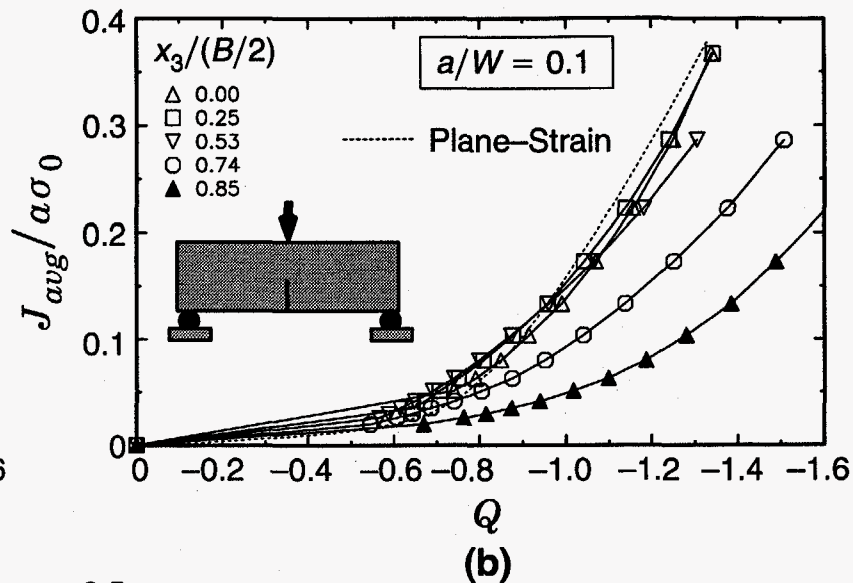
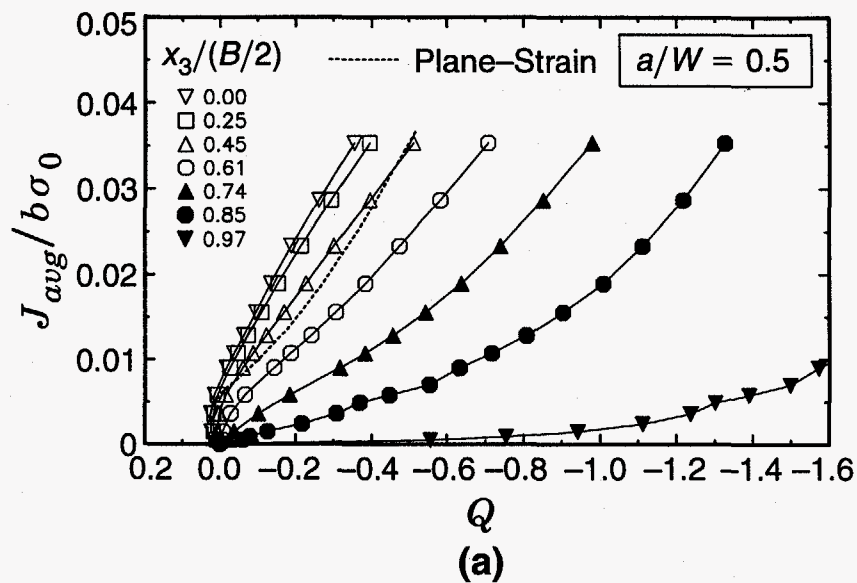


Fig. 7. Constraint in terms of Q triaxiality parameter for plane-sided, deep and shallow notch SE(B) specimens having $W/B=1$, $n=10$. (a) and (b) show variations across crack front for Q defined at $r/(J/\sigma_0)=2$. (c) and (d) show typical dependence of Q on distance ahead of crack tip. $E/\sigma_0=500$, $\nu=0.3$ in all analyses.

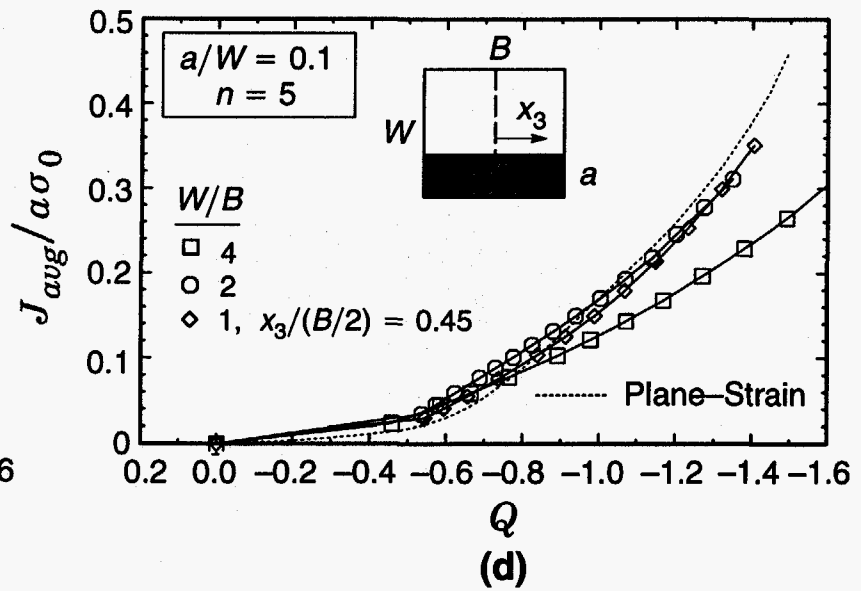
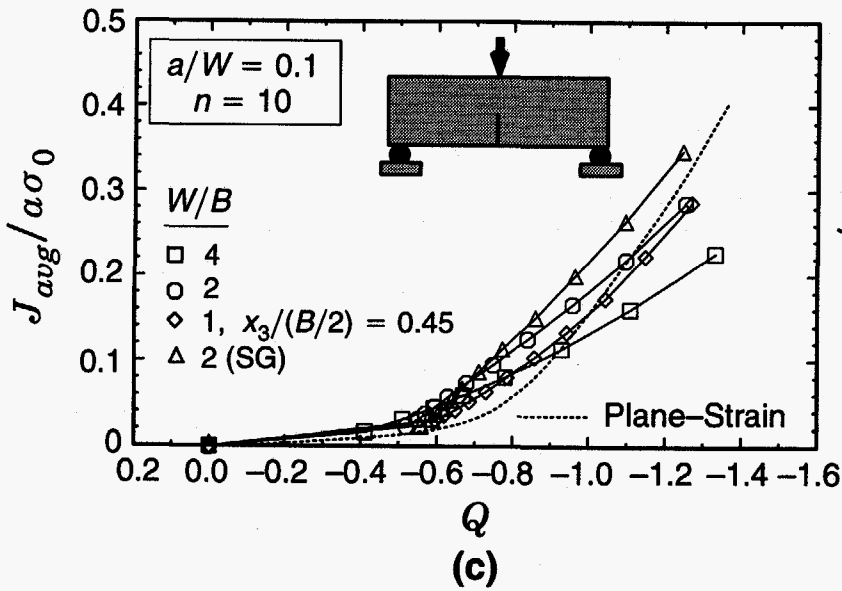
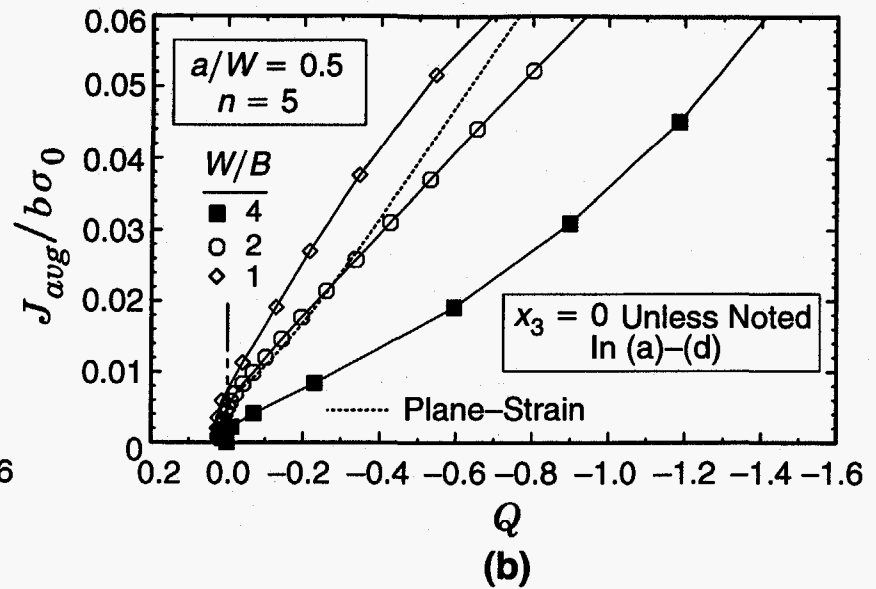
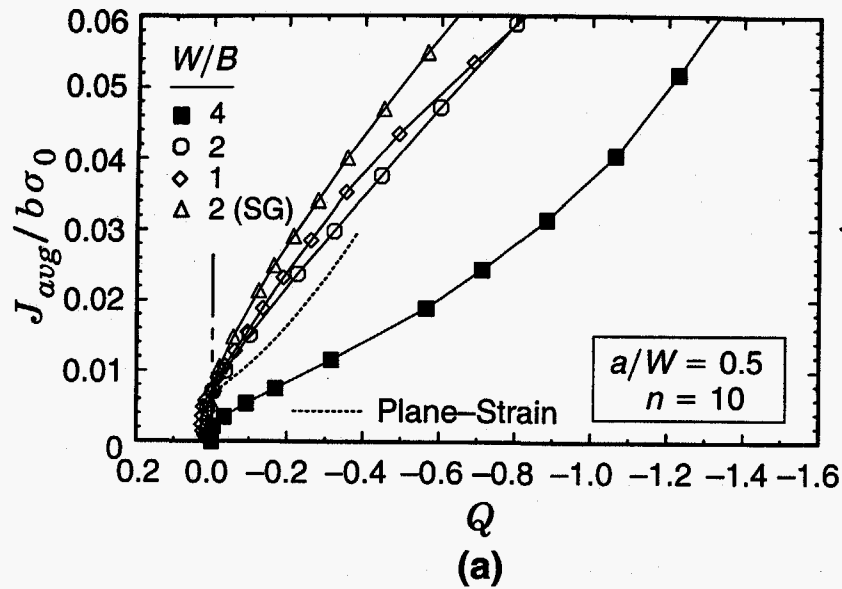


Fig. 8. J - Q trajectories for SE(B) specimens showing effects of a/W ratio, B/W ratio, side-grooves and strain hardening. Q defined at $r/(J/\sigma_0) = 2$ and $E/\sigma_0 = 500$, $\nu = 0.3$ in all analyses.

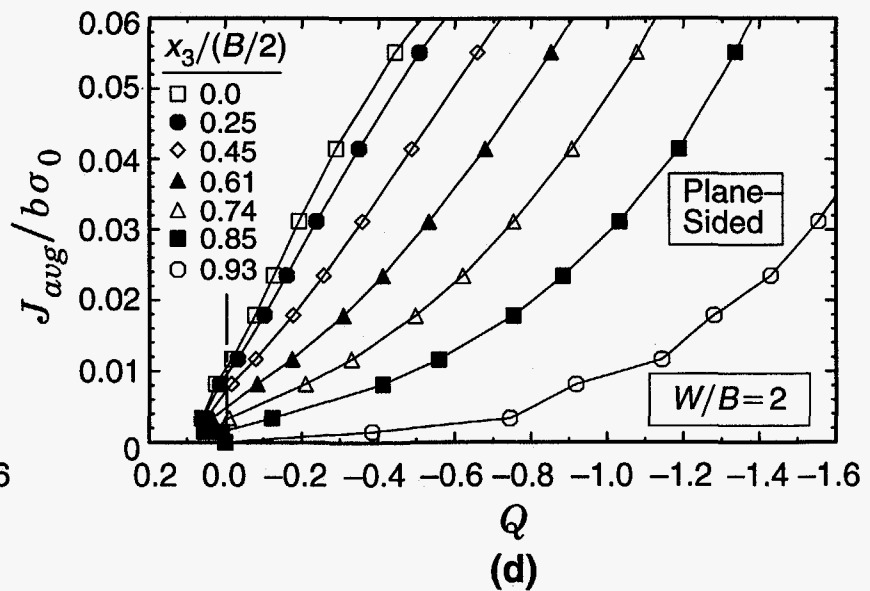
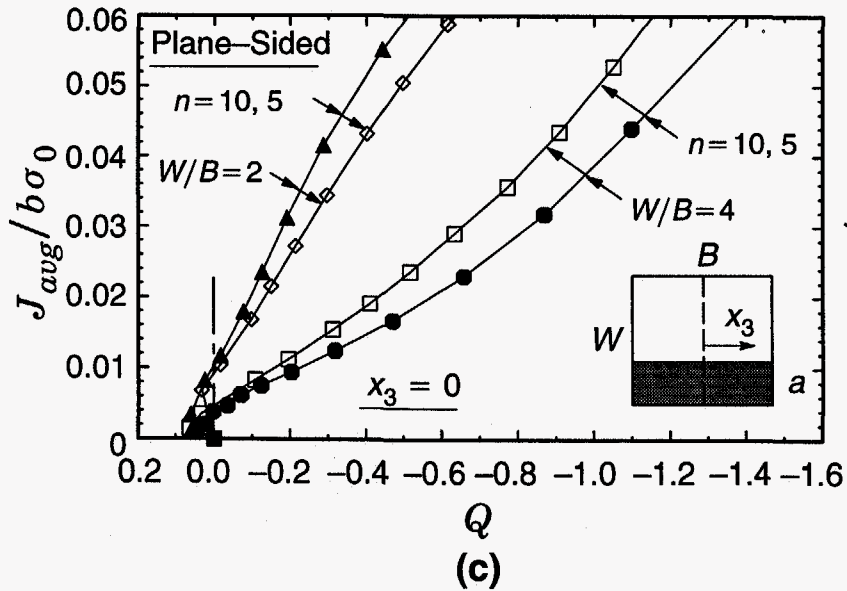
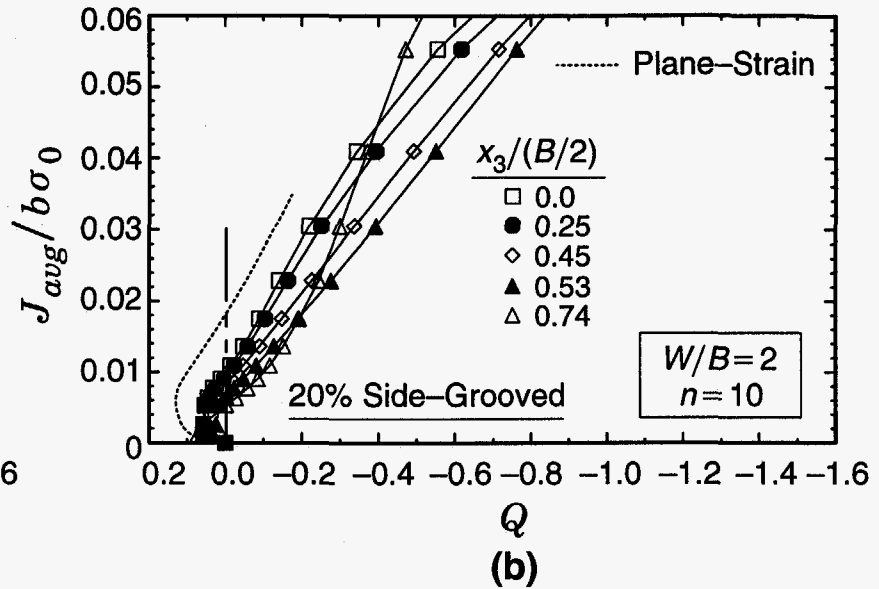
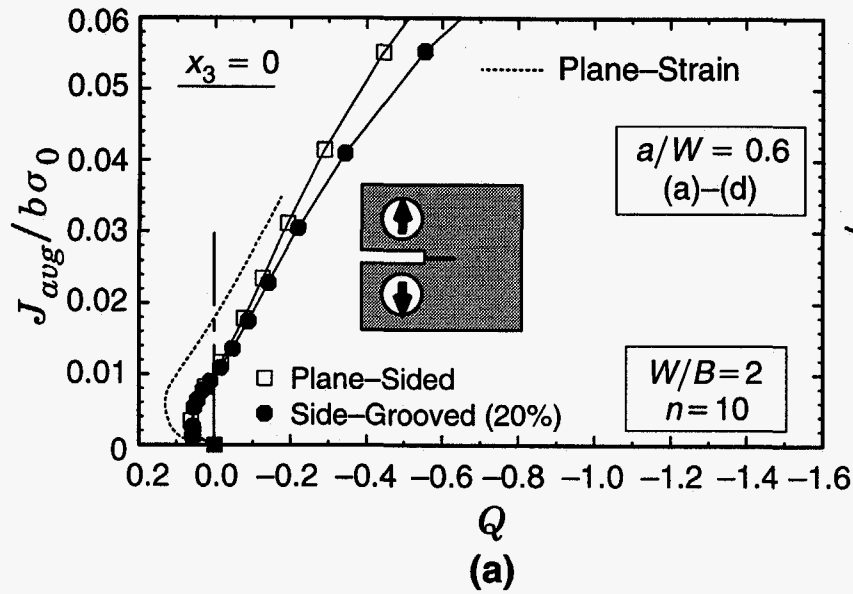
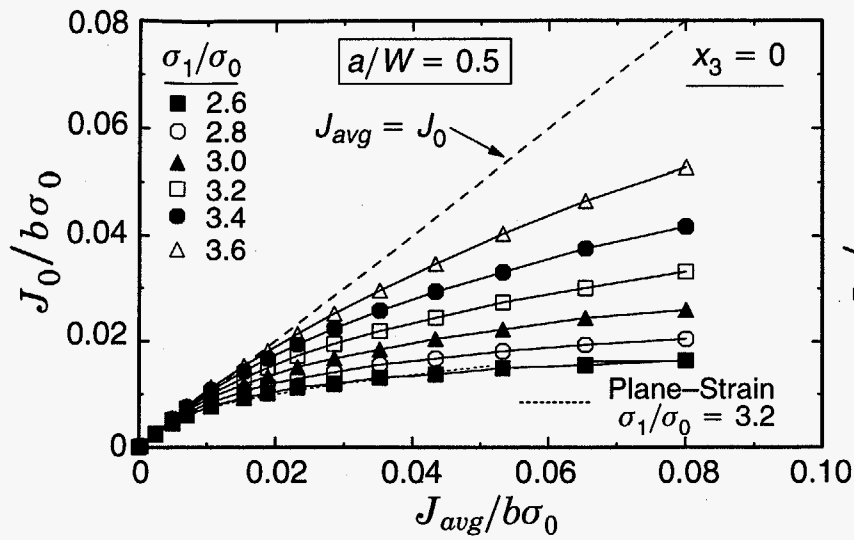
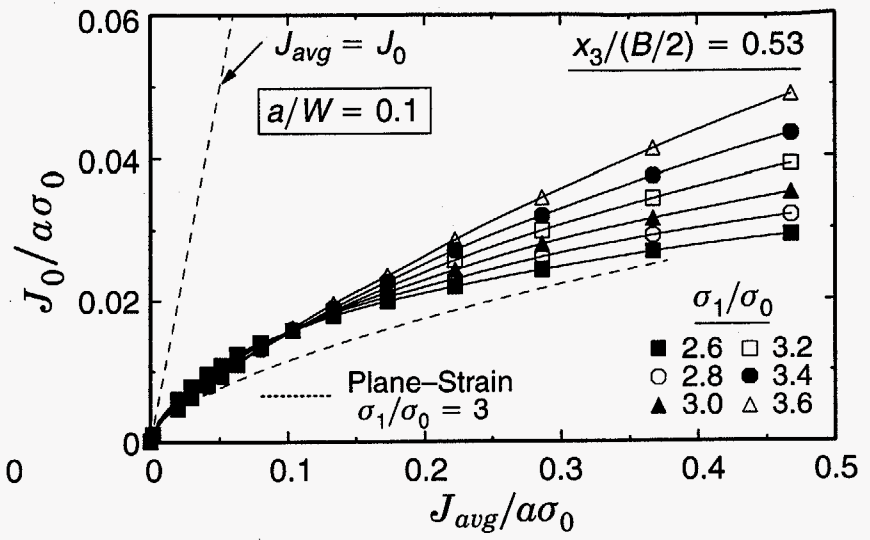


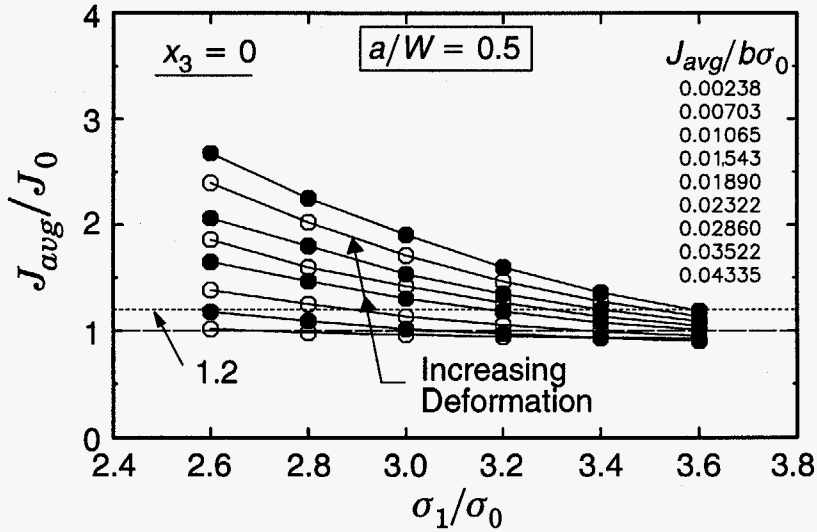
Fig. 9. J - Q trajectories for C(T) specimens showing effects of B/W ratio, side-grooves and strain hardening. Q defined at $r/(J/\sigma_0) = 2$ and $E/\sigma_0 = 500$, $\nu = 0.3$ in all analyses.



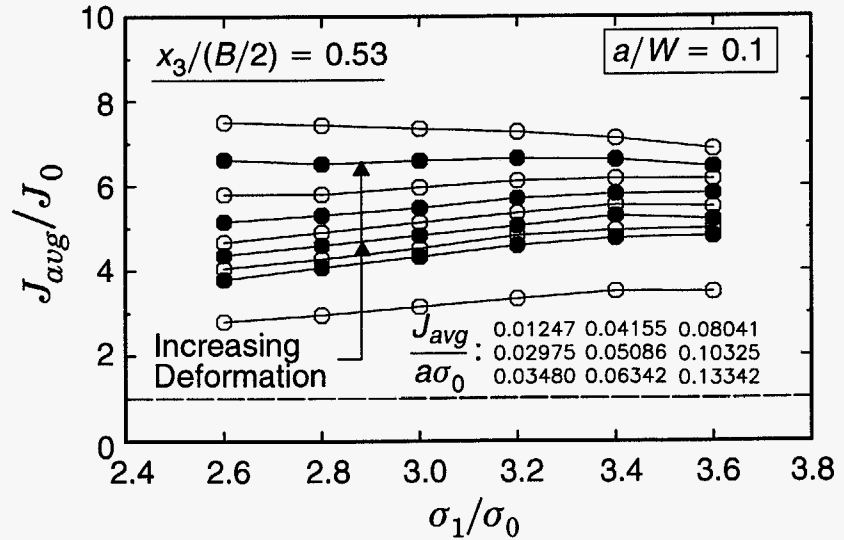
(a)



(b)

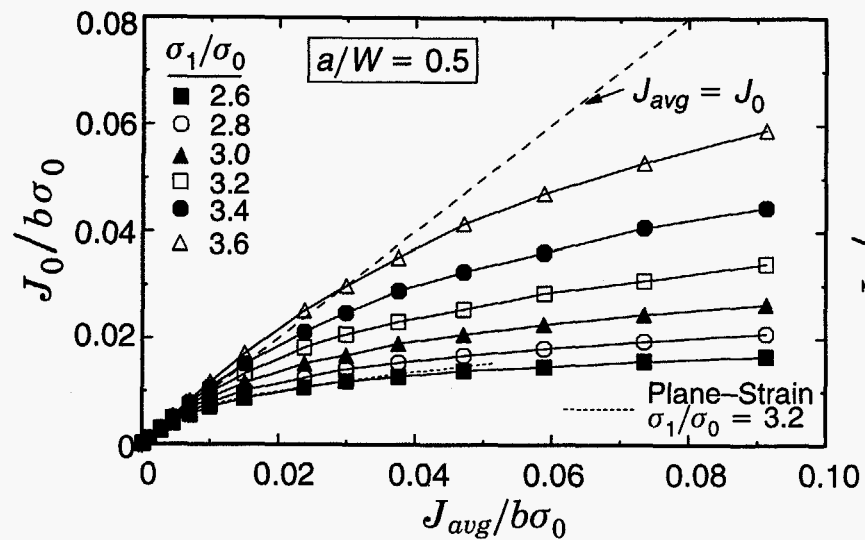


(c)

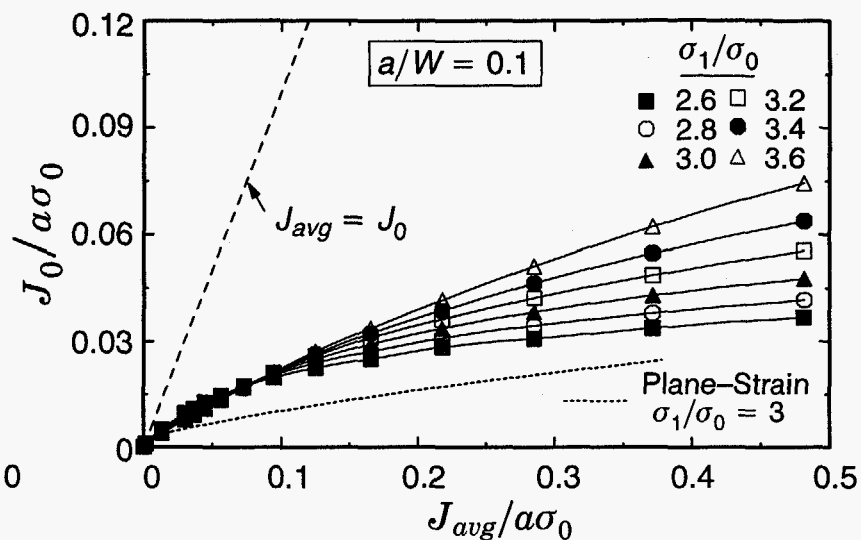


(d)

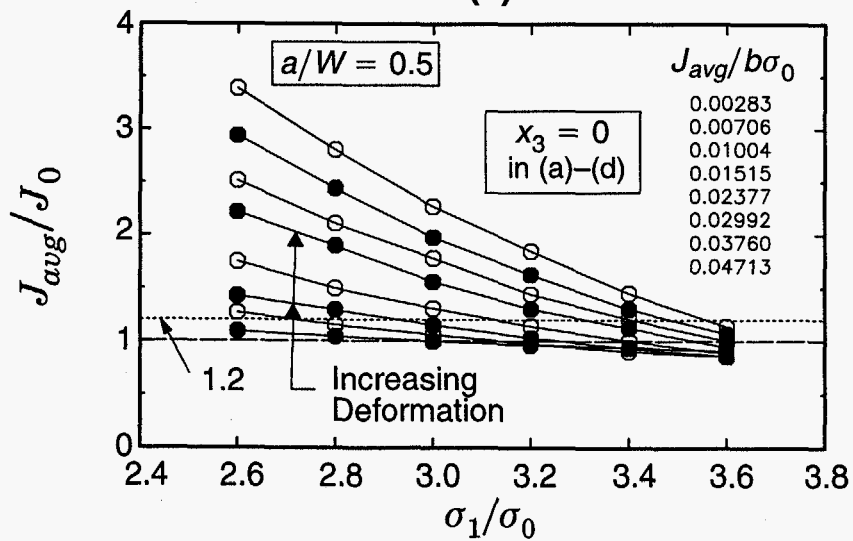
Fig. 10. Constraint in terms of the toughness scaling model for plane-sided, deep and shallow notch SE(B) specimens having $W/B=1$, $n=10$. (a) and (b) show variations across crack front. (c) and (d) show corresponding dependence of toughness scaling ratio on specified principal stress value. $E/\sigma_0=500$, $\nu=0.3$ in all analyses.



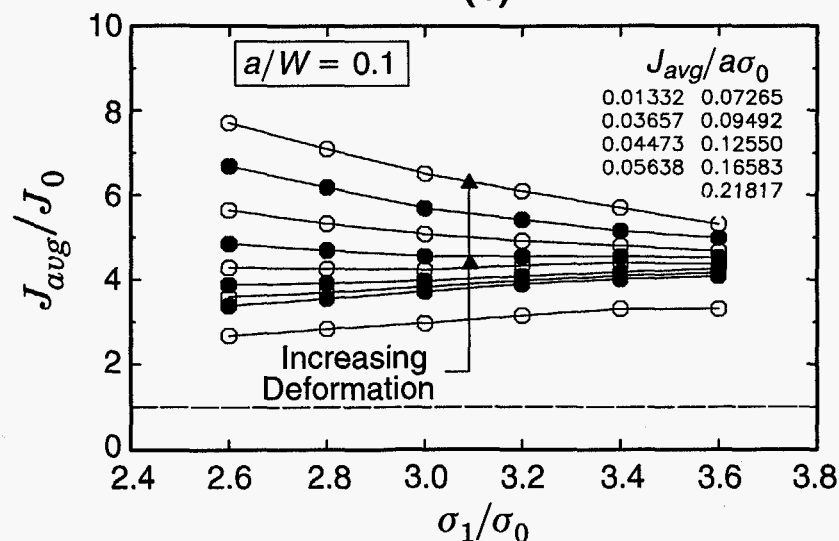
(a)



(b)



(c)



(d)

Fig. 11. Constraint in terms of the toughness scaling model for plane-sided, deep and shallow notch SE(B) specimens having $W/B=2$, $n=10$. (a) and (b) show variations across crack front. (c) and (d) show corresponding dependence of toughness scaling ratio on specified principal stress value. $E/\sigma_0=500$, $\nu=0.3$ in all analyses.

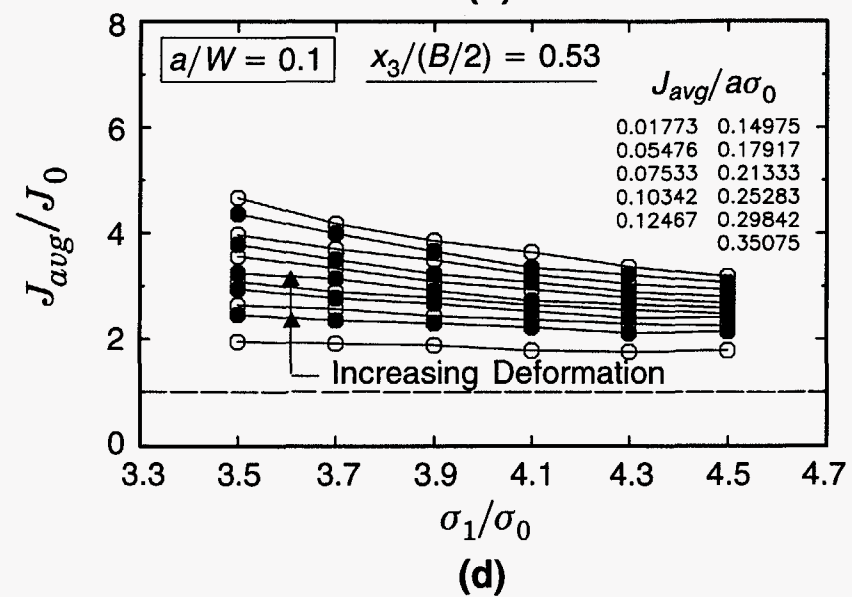
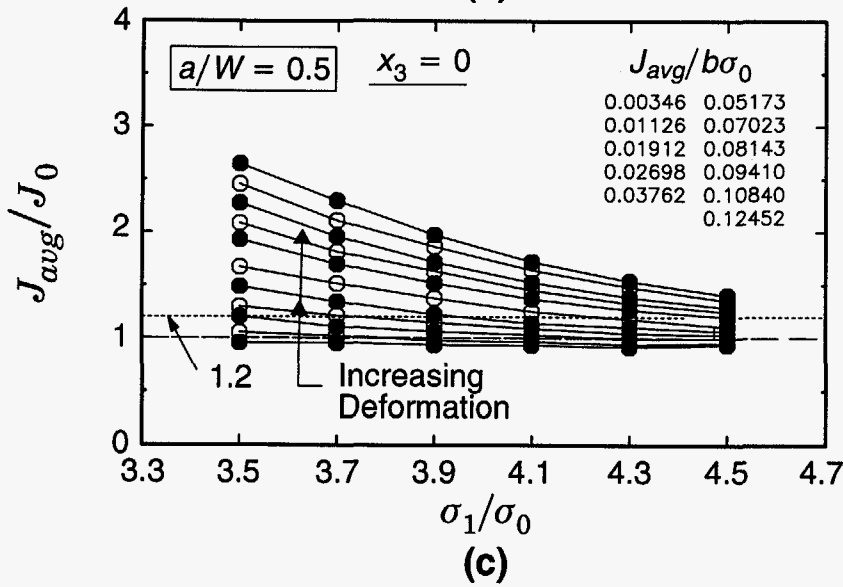
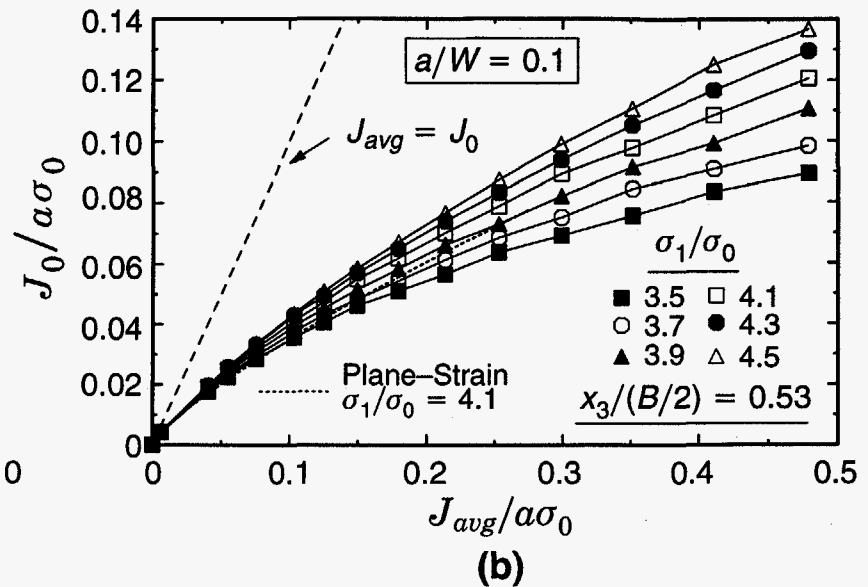
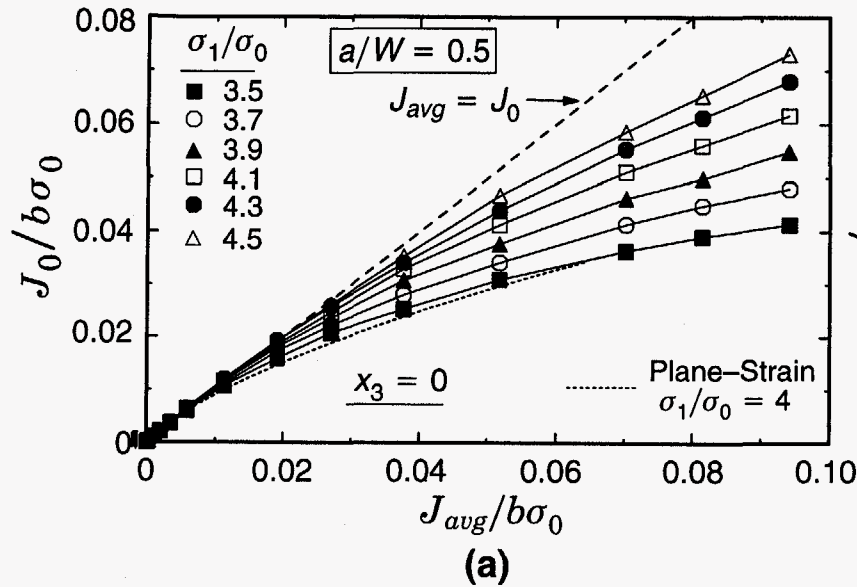
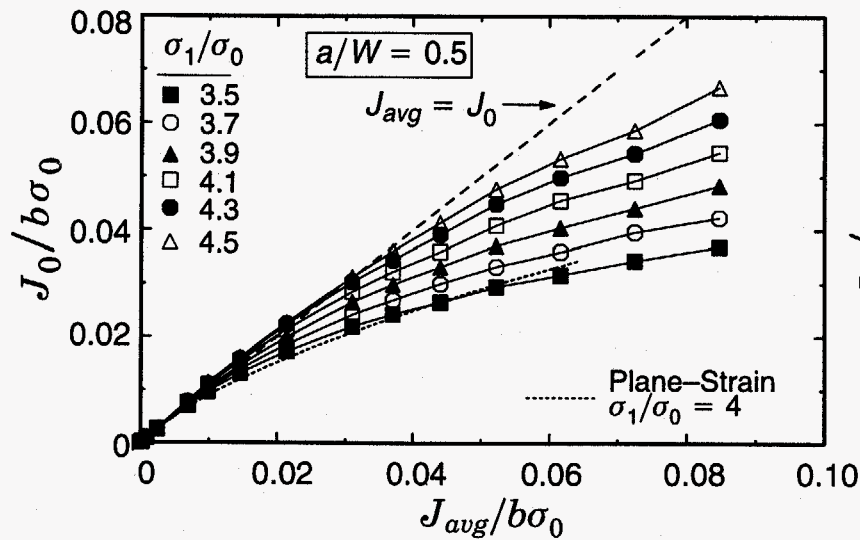
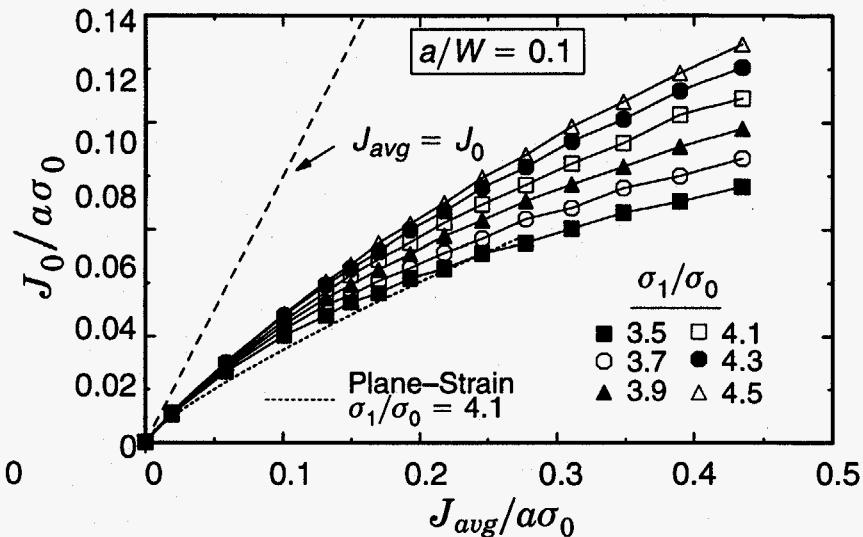


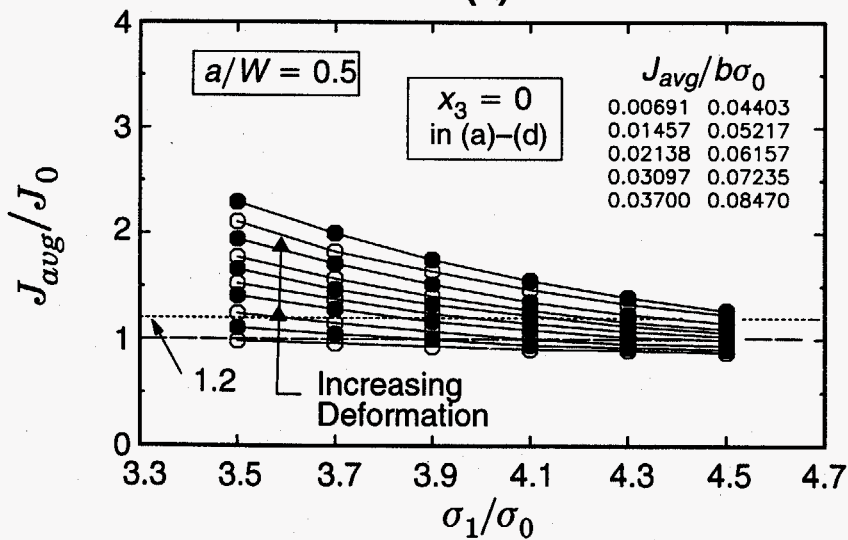
Fig. 12. Constraint in terms of the toughness scaling model for plane-sided, deep and shallow notch SE(B) specimens having $W/B = 1$, $n = 5$. (a) and (b) show variations across crack front. (c) and (d) show corresponding dependence of toughness scaling ratio on specified principal stress value. $E/\sigma_0 = 500$, $\nu = 0.3$ in all analyses



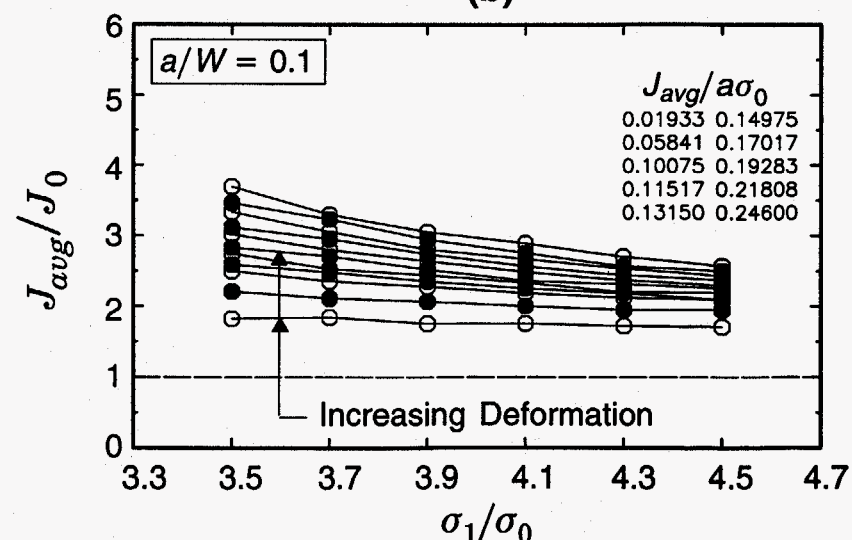
(a)



(b)



(c)



(d)

Fig. 13. Constraint in terms of the toughness scaling model for plane-sided, deep and shallow notch SE(B) specimens having $W/B=2$, $n=5$. (a) and (b) show variations across crack front. (c) and (d) show corresponding dependence of toughness scaling ratio on specified principal stress value. $E/\sigma_0=500$, $\nu=0.3$ in all analyses.

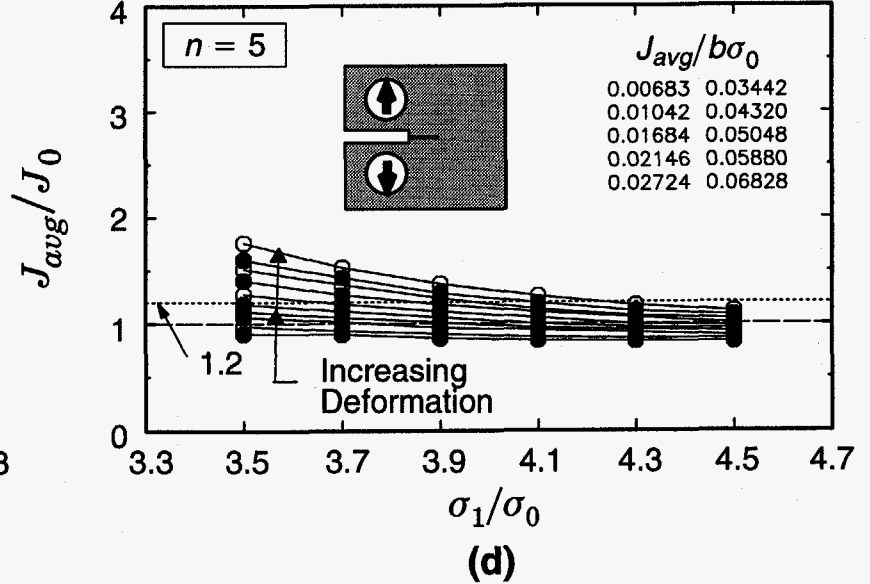
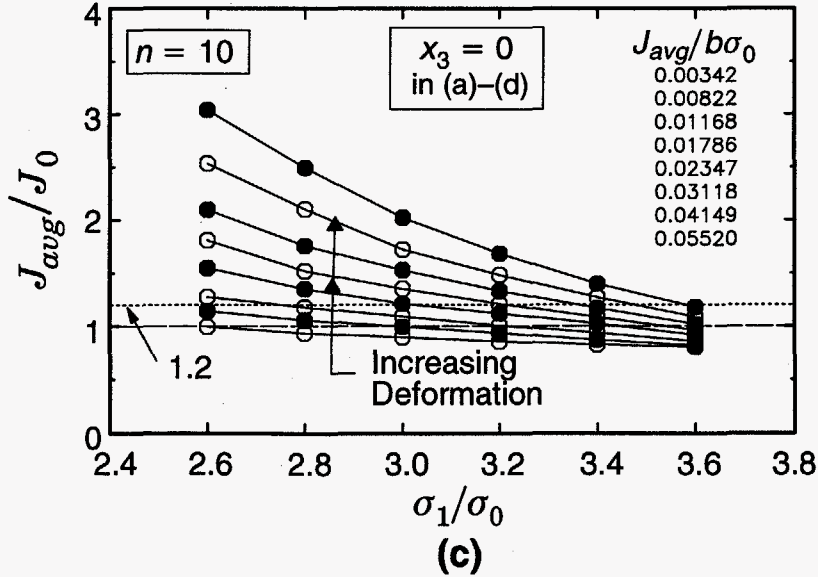
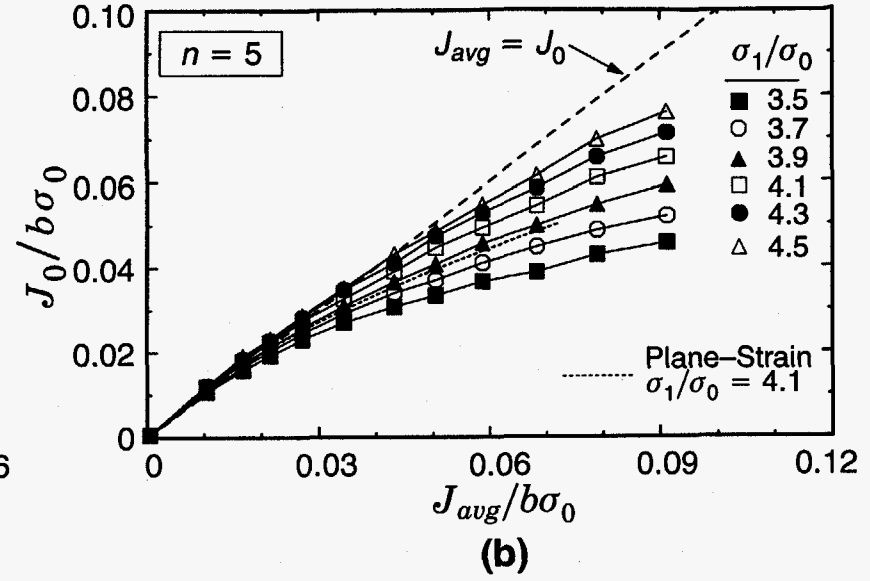
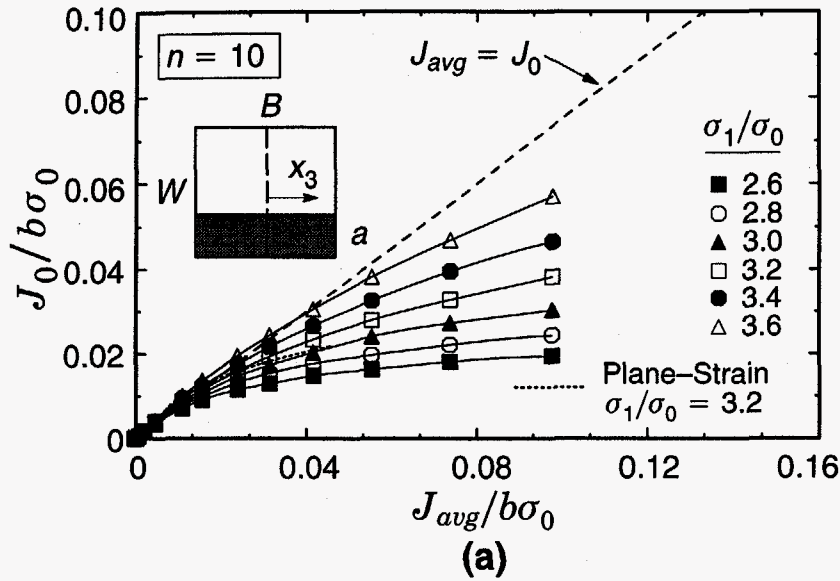


Fig. 14. Constraint in terms of the toughness scaling model for plane-sided C(T) specimens having $W/B=2$, $a/W=0.6$. (a) and (b) show variations across crack front. (c) and (d) show corresponding dependence of toughness scaling ratio on specified principal stress value. $E/\sigma_0=500$, $\nu=0.3$ in all analyses.

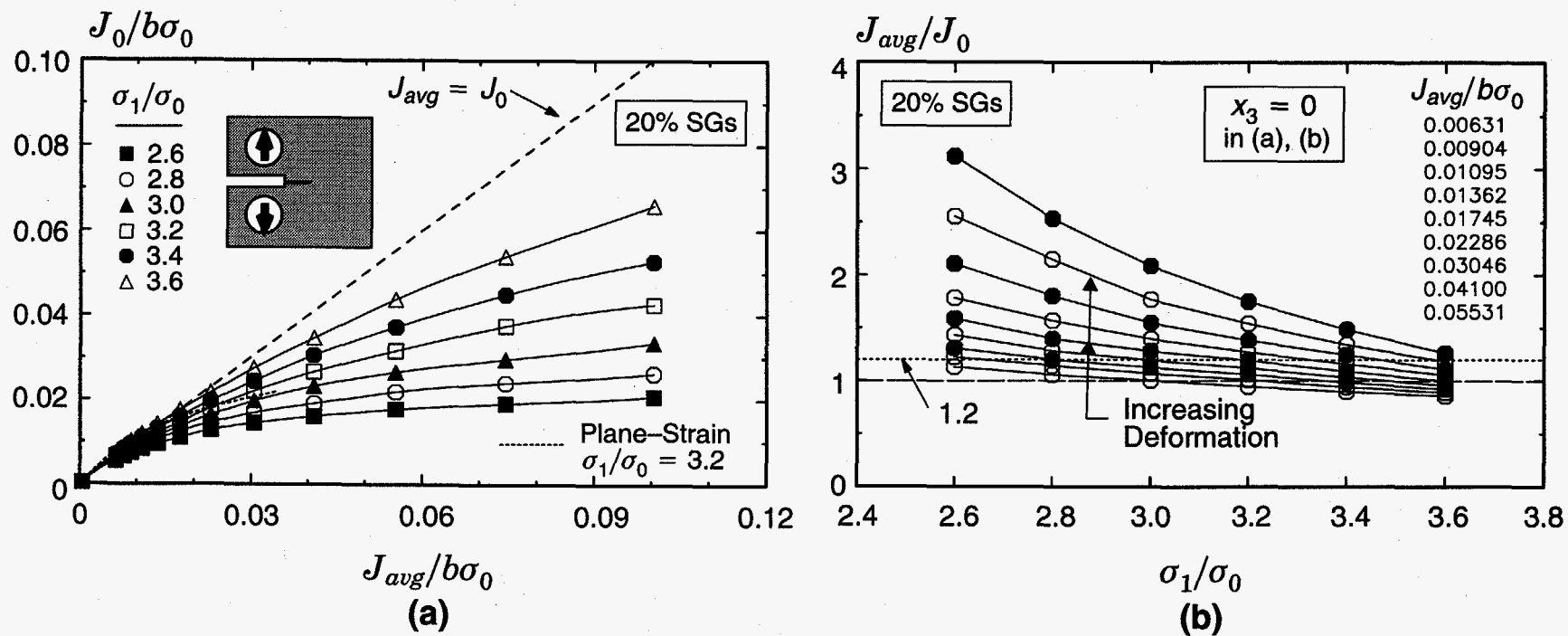


Fig. 15. Constraint in terms of the toughness scaling model for 20% side-grooved C(T) specimens having $W/B=2$, $a/W=0.6$. (a) shows variations across crack front. (b) shows corresponding dependence of toughness scaling ratio on specified principal stress value. $E/\sigma_0=500$, $\nu=0.3$ in all analyses.

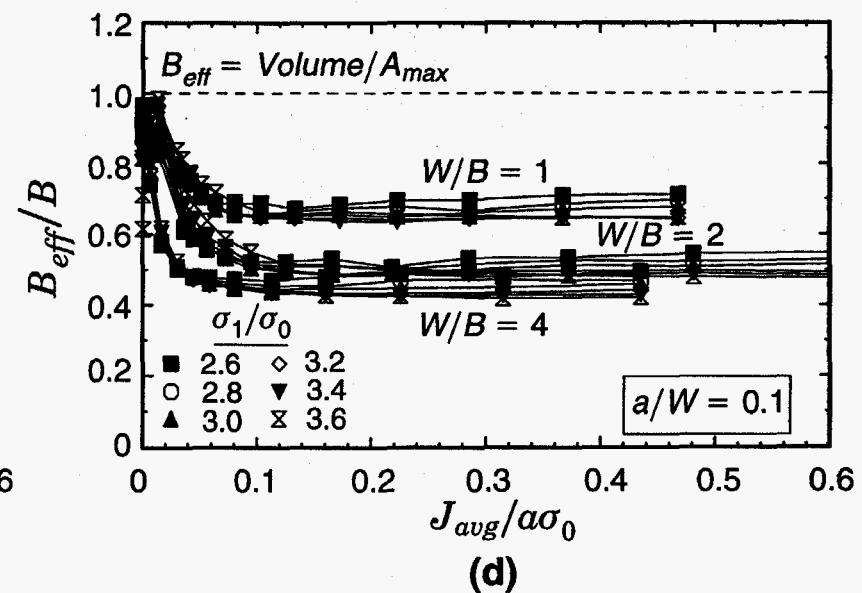
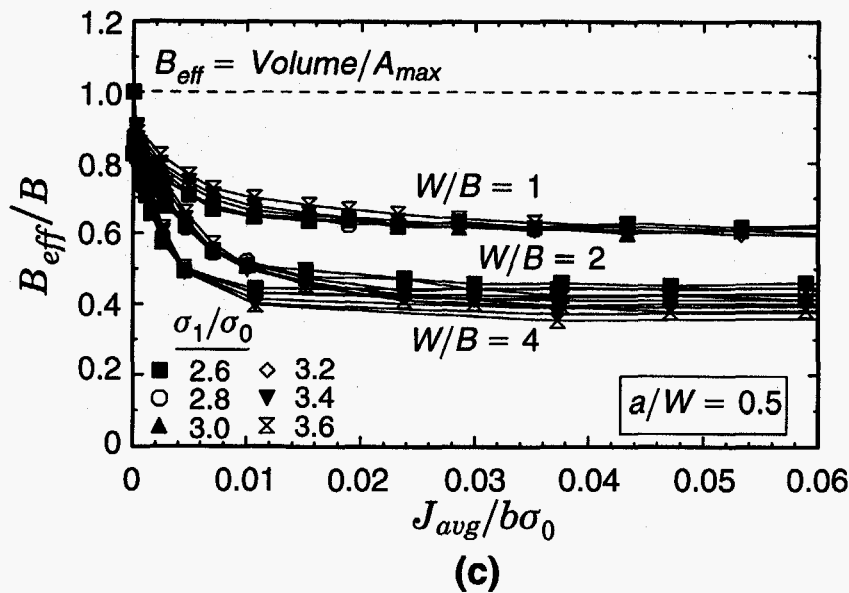
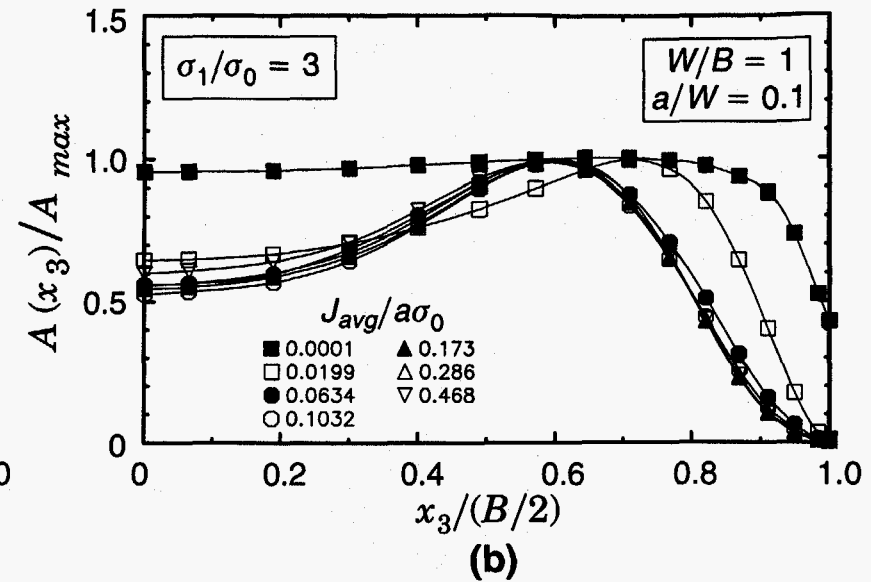
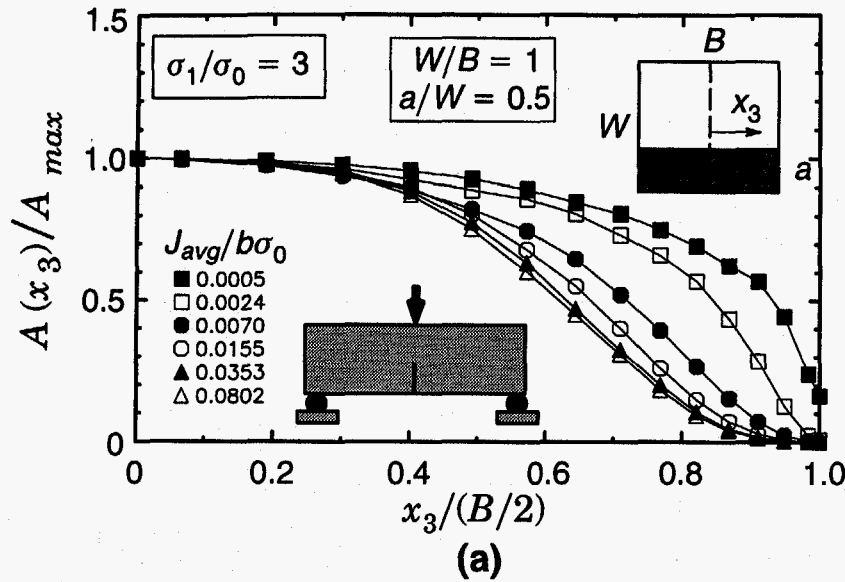


Fig. 16. Areas within a principal stress contour across the crack front (a), (b) for plane-sided SE(B) specimens with $n = 10$. Effective thicknesses for deep and shallow notch configurations over a range of thicknesses and principal stress ratios (c), (d). $E/\sigma_0 = 500$, $\nu = 0.3$ in all analyses.

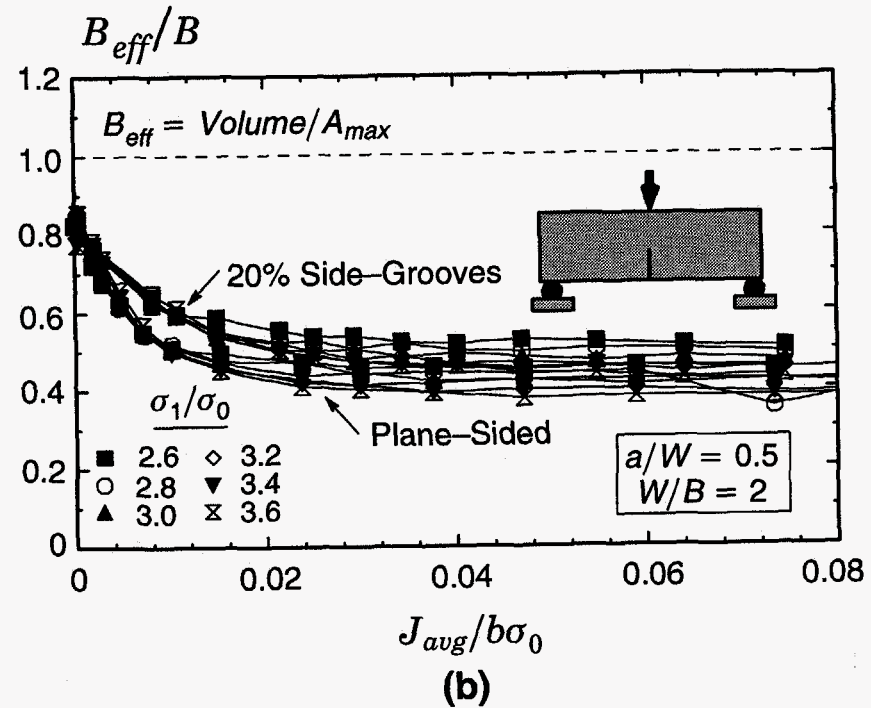
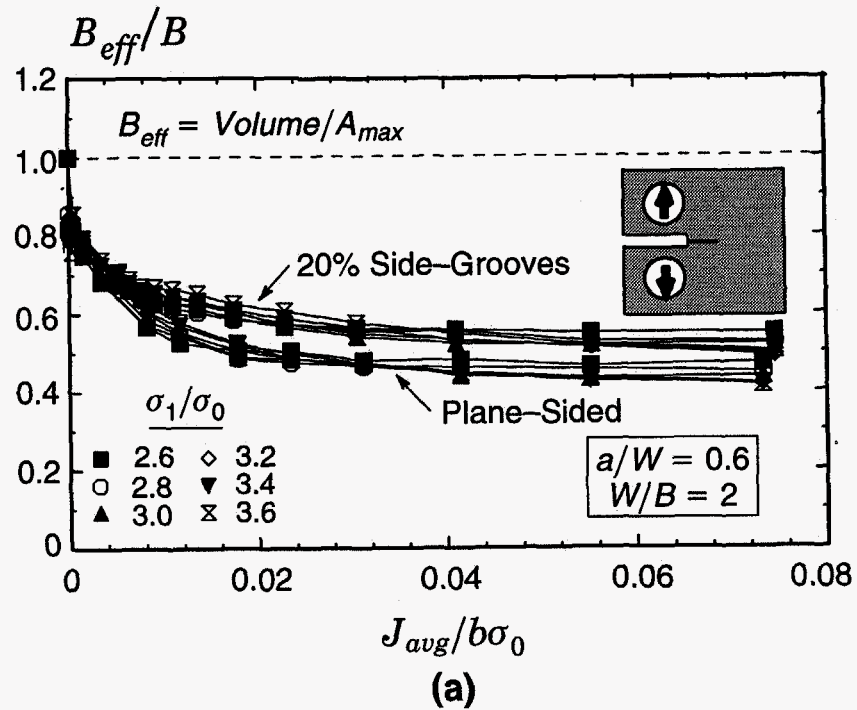


Fig. 17. Effective thicknesses for deep notch C(T) and SE(B) specimens showing the effects of 20% side-grooves. $E/\sigma_0 = 500$, $\nu = 0.3$, $n = 10$ all analyses.

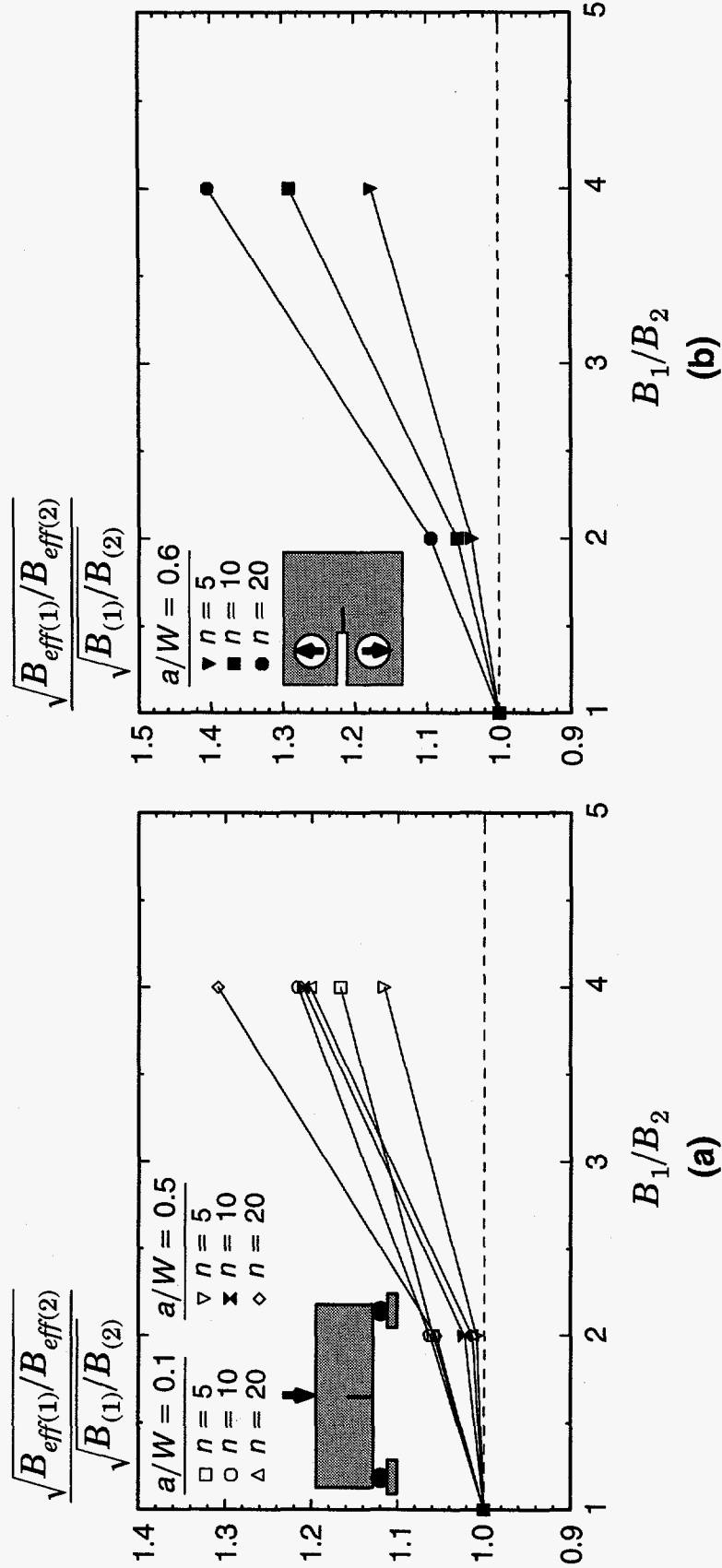


Fig. 18. Comparison of effective and actual thicknesses for plane-sided SE(B) and C(T) specimens. $E/\sigma_0 = 500$, $\nu = 0.3$.

BIBLIOGRAPHIC DATA SHEET

(See instructions on the reverse)

1. REPORT NUMBER
(Assigned by NRC. Add Vol., Supp., Rev.,
and Addendum Numbers, if any.)

NUREG/CR-6317

2. TITLE AND SUBTITLE

Numerical Investigation of 3-D Constraint Effects on Brittle
Fracture in SE(B) and C(T) Specimens

3. DATE REPORT PUBLISHED

MONTH	YEAR
July	1996

4. FIN OR GRANT NUMBER

J6036

5. AUTHOR(S)

Markku Nevalainen, Technical Research Centre of Finland (VTT)
Robert H. Dodds, Jr., University of Illinois

6. TYPE OF REPORT

Technical

7. PERIOD COVERED (Inclusive Dates)

Feb. 1994 - Feb. 1995

8. PERFORMING ORGANIZATION - NAME AND ADDRESS (If NRC, provide Division, Office or Region, U.S. Nuclear Regulatory Commission, and mailing address; if contractor, provide name and mailing address.)

University of Illinois at Urbana Champaign
Department of Civil Engineering, MC-250
205 North Mathews Avenue
Urbana, IL 61801

Under Contract to:
Naval Surface Warfare Center
3-A Leggett Circle, Code 614
Annapolis, MD 21402-5067

9. SPONSORING ORGANIZATION - NAME AND ADDRESS (If NRC, type "Same as above"; if contractor, provide NRC Division, Office or Region, U.S. Nuclear Regulatory Commission, and mailing address.)

Division of Engineering Technology
Office of Nuclear Regulatory Research
U.S. Nuclear Regulatory Commission
Washington, DC 20555-0001

10. SUPPLEMENTARY NOTES

Shah N.M. Malik, NRC Project Manager

11. ABSTRACT (200 words or less)

This investigation employs 3-D nonlinear finite element analyses to conduct an extensive parametric evaluation of crack front stress triaxiality for deep notch SE(B) and C(T) specimens and shallow notch SE(B) specimens, with and without side grooves. Crack front conditions are characterized in terms of J-Q trajectories and the constraint scaling model for cleavage fracture toughness proposed previously by Dodds and Anderson. The 3-D computational results imply that a significantly less strict size/deformation limits indicated by previous plane-strain computations, relative to the limits indicated by previous plane strain computations, is needed to maintain small-scale yielding conditions at fracture by a stress-controlled cleavage mechanism in deep notch SE(B) and C(T) specimens. Additional new results made available from the 3-D analyses also include revised η -plastic factors for use in experimental studies to convert measured work quantities to thickness average and maximum (local) J-values over the crack front.

12. KEY WORDS/DESCRIPTORS (List words or phrases that will assist researchers in locating the report.)

Cleavage, Constraint, Ductile-to-Brittle Transition, Fracture Toughness, 3-D Finite Element Analysis, SE(B) Specimen, C(T) Specimen

13. AVAILABILITY STATEMENT

Unlimited

14. SECURITY CLASSIFICATION

(This Page)

Unclassified

(This Report)

Unclassified

15. NUMBER OF PAGES

16. PRICE